A Physically-based, Meshless Lagrangian Approach to Simulate Melting Precipitation

Craig Pelissier,[a,d] William Olson,[c,d] Kwo-Sen Kuo,[b,c] Adrian Loftus,[d] Robert Schrom,[d,e] Ian Adams,[d]

[a] *Science Systems and Applications Incorporated, Lanham, Maryland*

[b] *Earth System Science Interdisciplinary Center, University of Maryland College Park, College Park, Maryland*

[c] *Goddard Earth Sciences Technology and Research II, University of Maryland Baltimore County, Baltimore, Maryland*

[d] *NASA Goddard Space Flight Center, Greenbelt, Maryland*

[e] *Oak Ridge Associated Universities, Oak Ridge, TN*

Corresponding author: Craig Pelissier, craig.s.pelissier@nasa.gov

ABSTRACT: An outstanding challenge in modeling the radiative properties of stratiform rain systems is an accurate representation of the mixed-phase hydrometeors present in the melting layer. The use of ice spheres coated with meltwater or mixed-dielectric spheroids have been used as rough approximations, but more realistic shapes are needed to improve the accuracy of the models. Recently, realistically structured synthetic snowflakes have been computationally generated, with radiative properties that were shown to be consistent with coincident airborne radar and microwave radiometer observations. However, melting such finely-structured ice hydrometeors is a challenging problem, and most of the previous efforts have employed heuristic approaches. In the current work, physical laws governing the melting process are applied to the melting of synthetic snowflakes using a meshless-Lagrangian computational approach henceforth referred to as the Snow Meshless Lagrangian Technique (SnowMeLT). SnowMeLT is capable of scaling across large computing clusters, and a collection of synthetic aggregate snowflakes from NASA's OpenSSP database with diameters ranging from 2–10.5 mm are melted as a demonstration of the method. To properly capture the flow of meltwater, the simulations are carried out at relatively high resolution (15 μm), and a new analytic approximation is developed to simulate heat transfer from the environment without the need to simulate the atmosphere explicitly.

1. Background and Motivation

Over the span of several decades leading up to the present, a great number of observational and theoretical studies of melting precipitation have been carried out, motivated by the expectation that an improved knowledge of the properties and distributions of melting hydrometeors could have impacts on remote sensing, communications, and weather prediction. Early studies of melting precipitation, in particular, emphasized *in situ* or laboratory observations of individual snow particles (Knight 1979; Matsuo and Sasyo 1981; Rasmussen and Pruppacher 1982; Rasmussen et al. 1984; Fujiyoshi 1986; Oraltay and Hallett 1989, 2005; Mitra et al. 1990; Misumi et al. 2014; Hauk et al. 2016). These studies revealed characteristic phases of hydrometeor melting, starting with minute drops forming at the tips of fine ice structures, followed by movement of liquid by the action of surface tension toward linkages between these structures; then to complete melting of the fine structures and flow of meltwater to the junctions of coarser ice structures, and finally to the collapse of the main ice frame and meltwater forming a drop shape (Mitra et al. 1990). Complementary field observations have provided information regarding the vertical structure and bulk properties of melting hydrometeor layers (Leary and Houze 1979; Stewart et al. 1984; Willis and Heymsfield 1989; Fabry and Zawadzki 1995; Heymsfield et al. 2002, 2015, 2021; Tridon et al. 2019; Mróz et al. 2021). These studies inferred the role of hydrometeor self-collection, leading to larger aggregates of ice crystals with relatively low fall speeds above the freezing level in stratiform precipitation events. In the early stages of melting just below the freezing level, these snowflakes produce a peak of high radar reflectivity, followed by a decrease of reflectivity within a few hundred meters of the freezing level as the melting hydrometeors ultimately collapse into raindrops and acquire greater fall speeds.

In parallel, several models of hydrometeor melting have been developed, including those in which the initial ice hydrometeors were assumed to be spheroidal (Mason 1956; Yokoyama and Tanaka 1984; Klaassen 1988; D'Amico et al. 1998; Szyrmer and Zawadzki 1999; Bauer et al. 2000; Olson et al. 2001; Battaglia et al. 2003), and those where realistically-structured, non-spherical ice geometries were assumed initially (Botta et al. 2010; Ori et al. 2014; Johnson et al. 2016; Leinonen and von Lerber 2018). However, of the latter, only Leinonen and von Lerber (2018) applied physical laws in their melting simulations. Numerous additional studies either relied upon previously-developed melting models or used heuristic descriptions of melting hydrometeors as

the basis for calculating hydrometeor microwave scattering properties (Meneghini and Liao 1996, 2000; Russchenberg and Ligthart 1996; Fabry and Szyrmer 1999; Walden et al. 2000; Marzano and Bauer 2001; Adhikari and Nakamura 2004; Liao and Meneghini 2005; Zawadzki et al. 2005; Liao et al. 2009; Tyynelä et al. 2014; von Lerber et al. 2014). Generally speaking, the models developed in the aforementioned investigations can be used to reproduce the basic radar characteristics of melting layers, but there are quantitative differences in the simulated attenuation and backscatter that can be linked to assumptions regarding each modeled hydrometeor's environment, geometry and fall speed, internal meltwater distribution, aggregation/breakup, and derived dielectric properties.

Regarding applications of our knowledge of melting hydrometeor physics, it is understood that the relatively strong attenuation by melting precipitation is likely to have a greater influence on wireless and satellite communication systems, as less congested, higher-frequency bands are being exploited in these systems (Zhang et al. 1994; Panagopoulos et al. 2004; Siles et al. 2015). In numerical simulations of weather systems, melting precipitation contributes to a latent cooling of the environment that can have dynamical impacts (Lord et al. 1984; Szeto et al. 1988; Tao et al. 1995; Barth and Parsons 1996; Szeto and Stewart 1997; Unterstrasser and Zängl 2006; Phillips et al. 2007) and different parameterizations of melting hydrometeor microphysics can lead to different distributions of precipitation types at ground level (Thériault et al. 2010; Frick et al. 2013; Geresdi et al. 2014; Planche et al. 2014; Loftus et al. 2014; Cholette et al. 2020). However, explicit descriptions of partially melted hydrometeors in the microphysics schemes of prediction models are a relatively recent development, and improvements in both the representation of melting hydrometeors and the assimilation of melting-layer-affected reflectivities and radiances should be anticipated.

Simulating melting precipitation is challenging because it involves complex time-varying boundaries, multiple phases, contact forces, as well as fluid processes that progress at a time scale much smaller than the time scale of melting. To simulate the melting process rigorously requires a numerical method to approximate continuum physics equations that are generally expressed in the form of partial differential equations (PDEs). The complexity of the boundaries makes traditional finite-difference, finite-element, or finite-volume approaches difficult or intractable to apply. In contrast, the meshless-Lagrangian particle-based approach commonly referred to as Smoothed Particle Hydrodynamics (SPH) can handle deformable boundaries readily and provides a gen-

eral prescription for encoding continuum physics equations into the particle dynamics. SPH was first introduced (independently) by Gingold and Monaghan (1977) and Lucy (1977) to simulate astrophysical phenomena. Since then, among others applications, it has been used extensively to simulate complex fluid-flows and heat conduction. Examples of the use of SPH to simulate melting ice can be found in computer graphics, and in a preliminary investigation, we explored the adaptation of the approach of Iwasaki et al. (2010) to melt snowflakes (Kuo and Pelissier 2015). Motivated by this and earlier studies, and to gain a more complete understanding of the physics of melting precipitation, an SPH physics-based numerical method has been developed for simulating the evolving properties of fully three-dimensional melting hydrometeors with realistic shapes (snowflakes).

While SPH allows the microphysical processes of melting precipitation to be simulated directly from the corresponding continuum physics equations, the approach is compute intensive and requires parallel computing to be of practical use. To address this, an efficient numerical implementation, the Snow Meshless Lagrangian Technique (SnowMeLT), is developed that is capable of scaling across large computing clusters. In this work, SnowMeLT is used to melt snowflakes with diameters of up to ~ 1 cm at a resolution of 15 μm. This improves on the work of Leinonen and von Lerber (2018) where a resolution of 40 μm was used to melt snowflakes with diameters of up to 5.6 mm. The increase in resolution is particularly important for the types of synthetic snowflakes considered here, since they are composed of crystals that typically have a thickness of only about a hundred micrometers or less. SnowMeLT also incorporates recent advances that provide a more accurate treatment of free-surface flows. Another notable difference is the formulation of the heat transfer from the surrounding environment. To avoid the prohibitively large cost of simulating the surrounding environment, Leinonen and von Lerber (2018) simplified the conduction by disregarding the effects of the meltwater, and used the floating random walk approach of Haji-Sheikh and Sparrow (1966) to solve for the heat transfer between the ice surface and a far-field temperature value prescribed at some large radial distance from the center of the melting hydrometeor. Here, a method for specifying the heat transfer from the environment is developed using an SPH formulation of the heat conduction equation that includes conduction through the meltwater, and still avoids simulating the surrounding environment explicitly. The approach relies on the assumption of a uniform air temperature near to the hydrometeor, and a far-field thermal boundary condition

based on the steady-state conduction of heat through an environment with uniform conductivity and radial symmetry. Also different from Leinonen and von Lerber (2018), SnowMeLT uses a curvature-based surface-tension force derived directly from the continuum-surface-force (CSF) model and contact forces derived from Young's Equation, rather than the more heuristic approach of using (macroscopic) pair-wise attractive forces inspired by molecular cohesion models.

To demonstrate the applicability of SnowMelT, a set of eleven synthetic snowflakes are selected from the NASA OpenSSP database (Kuo et al. 2016) and melted. The selected hydrometeors are comprised of smaller individual "pristine" dendritic crystals that are aggregated to create snowflakes of larger sizes. Their diameters and masses range from 2.1 – 10.5 mm and 1.8 – 6.9 mg. The geometry of the selected synthetic snowflakes is quite complex and provides a good demonstration of the general applicability of SnowMeLT. Additionally, the single scattering properties of synthetic snowflakes from this database have been successfully used to improve the representation of snow in active/passive microwave remote sensing estimation methods for precipitation (Olson et al. 2016). In view of this, it is conceivable that mixed-phase hydrometeors generated by melting theses synthetic snowflakes could lead to improved electromagnetic modeling of the melting layer in remote sensing methods, and as a result, the work presented in this study also demonstrates the potential of SnowMeLT for these methods.

This paper is intended to be largely self-contained, with derivations of key equations provided in the appendices. In section 2, a brief description of SPH is given that introduces the key concepts and discusses challenges in its application to melting snowflakes, and in section 3, the formulation of the microphysics of SnowMeLT is developed in detail. In section 4, the deformation of a cube of water into a spherical drop and into a sessile drop on an ice slab is presented, as well as a comparison between SnowMeLT and a finite-difference, multi-shell approach for melting ice spheres, followed by the results for the aforementioned set of aggregate snowflakes. In section 5, the article concludes with an overview of the present implementation and the steps required to produce mixed-phased hydrometeors for the purpose of modeling the melting layers of stratiform precipitation events.

2. Smoothed Particle Hydrodynamics

While SPH was originally used to simulate fluid flows (as the name suggests), it provides a prescription for simulating almost *any* set of (coupled) partial differential equations (PDEs) and has been applied to a much larger class of phenomena since its conception. In contrast to methods that use approximate derivatives (e.g., a finite-difference) of continuum fields, SPH uses exact derivatives of approximate fields. Importantly, SPH is a meshless particle-based approach, and as such, can accommodate the time-varying boundaries of melting snowflakes — a crucial component that makes SPH a viable candidate for the present application. However, melting snowflakes with SPH has many challenges, especially the simulation of thin layers of meltwater. In section a, a brief description of SPH is given that introduces the particle interpretation of SPH, key concepts, and the notation used throughout the paper, while in section b, issues related to the simulation of thin layers of meltwater are discussed along with the approach used in this work.

a. A Brief Introduction to SPH

SPH is most intuitively understood as a particle-based approach in which fluids, gases, and solids are represented as a system of interacting point-particles or *SPH-particles*. However, its mathematical formulation is based on the use of an interpolating kernel to approximate continuum fields that evolve according to the underlying dynamics being simulated. As a result, SPH is most naturally described as an interpolating method, from which the particle interpretation follows as a consequence of formulating a suitable numerical algorithm. The aim of this section is to introduce the concepts required to formulate the microphysical processes described in section 3. A more in-depth introduction to SPH can be found in, e.g., Monaghan (1992).

The fundamental approximation in SPH is the use of an interpolation kernel to define interpolated or "smoothed" approximations of corresponding fields. As an example, the SPH-field for the density is given by

$$\langle \rho(\mathbf{r}) \rangle = \int_V \rho(\mathbf{r}') \mathcal{W}(\|\mathbf{r} - \mathbf{r}'\|, h)\, dV', \tag{1}$$

where $\mathcal{W}(|\mathbf{r} - \mathbf{r}'|, h)$ denotes the smoothing kernel, and $\langle \cdot \rangle$ has been used to indicate a smoothed field. The smoothing kernel is assumed to be positive, radially centered at $\mathbf{r}$, and monotonically

decreasing with $|\mathbf{r}-\mathbf{r}'|$ with a characteristic smoothing length, h, which determines the resolution of the SPH simulation. As the smoothing length vanishes, to recapture the original field, the smoothing kernel should have the property

$$\lim_{h\to 0} \mathcal{W}(\|\mathbf{r}-\mathbf{r}'\|, h) = \delta^3(\mathbf{r}-\mathbf{r}')\,. \tag{2}$$

Perhaps the most natural choice is the Gaussian kernel,

$$\mathcal{W}(\|\mathbf{r}-\mathbf{r}'\|, h) = \frac{1}{\pi^{3/2}h^3}\exp\left(\frac{-r^2}{h^2}\right), \tag{3}$$

which is well known to satisfy this condition and was the original choice made by Gingold and Monaghan (1977) and Lucy (1977). The form of the smoothing kernel is important for both computational and numerical reasons, and a significant amount of work has gone into the design of "good" kernels. In this work, we follow the recommendation of Dehnen and Aly (2012) and employ the Wendland C^2 kernel; see, appendix A.

To evaluate (numerically) the integral in Eq. (1), the smoothing kernel is truncated after an appropriate distance depending on how rapidly the kernel falls off. For the Wendland C^2 kernel, it is sufficient to approximate the integral with support out to one smoothing length. The density field in Eq. (1) then becomes

$$\langle\rho(\mathbf{r})\rangle \approx \int_\Omega \rho(\mathbf{r}')\mathcal{W}(\|\mathbf{r}-\mathbf{r}'\|, h)\,dV', \tag{4}$$

where Ω denotes the ball $B_h(\|\mathbf{r}-\mathbf{r}'\|) = \{\|\mathbf{r}-\mathbf{r}'\| : \|\mathbf{r}-\mathbf{r}'\| \le h\}$. This integral can now be approximated by the finite sum,

$$\langle\rho\rangle_i = \sum_{j\in\Omega} \rho_j \mathcal{W}_{ij}\,\Delta V_j\,, \tag{5}$$

where the positions for $\mathbf{r}$ and $\mathbf{r}'$ have been replaced with $\mathbf{r}_i$ and $\mathbf{r}_j$, respectively, and the notation $\langle\cdot\rangle_i$ is used to indicate a finite-sum approximation of an SPH-field. To simplify the notation, the density field, $\rho(\mathbf{r}_i)$, and smoothing kernel, $\mathcal{W}(\|\mathbf{r}-\mathbf{r}'\|, h)$, are written as ρ_i and $\mathcal{W}_{ij}$. Noticing

$\rho_j \Delta V_j$ equals the mass contained in the volume ΔV_j, the density can be expressed as

$$\langle \rho \rangle_i = \sum_{j \in \Omega} m_j \mathcal{W}_{ij} \,. \tag{6}$$

This form implies the particle interpretation of SPH. Namely, the interpolating points are considered to be point-mass particles or SPH-particles with fields, such as the density field, computed by taking an average over nearby SPH-particles. Here we have used the density field as an example. In general, SPH-fields are approximated by,

$$\langle f \rangle_i = \sum_{j \in \Omega} f_j \mathcal{W}_{ij} \, \Delta V_j \,, \tag{7}$$

and their derivatives can be computed analytically in terms of the derivatives of the smoothing kernel (see appendix A).

In SPH, the dynamics of the system are determined by prescribing SPH-particle interactions derived from the underlying equations of the physical processes being simulated. In section 3, the formulation of the dynamics of SnowMeLT is described in detail.

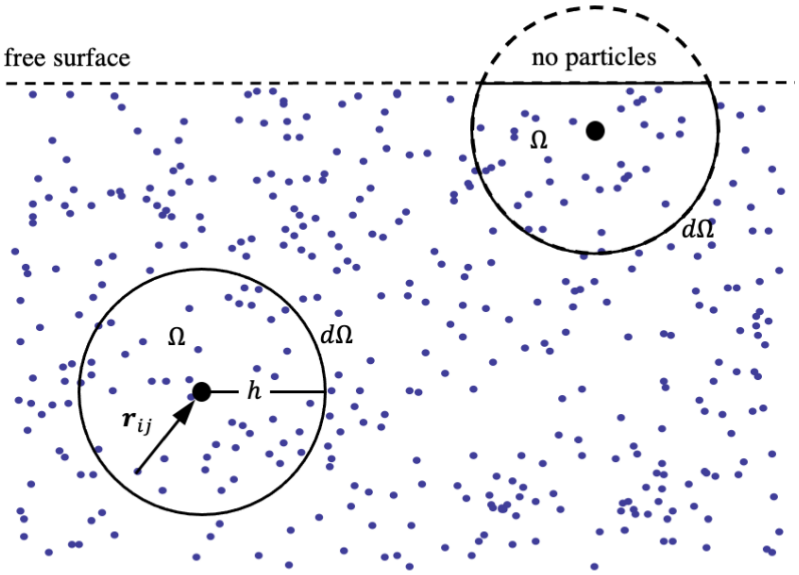

FIG. 1. Depiction of the SPH averaging volume (Ω) and surface ($d\Omega$) in the interior and at the free surface.

b. Thin Layers of Meltwater and Free-Surface Flows

One of the challenges of using SPH to melt snowflakes is simulating the free-surface flow of thin layers of meltwater. Free-surface flows are characterized by the presence of an evolving interface between liquid and air where there are no surface-parallel stresses. Imposing boundary conditions and maintaining an accurate interpolation near a free surface is difficult in SPH. In many applications, for example dam break simulations, the free surface has little effect on the overall dynamics since the surface of the fluid is comparatively small, and as a result, as long as the surface dynamics are not of particular interest, it is not a significant concern. However, free-surface flows are critical when simulating the movement of thin layers of meltwater on the ice structures of melting precipitation. The main difficulty arises from the absence of SPH-particles on one side of the surface that leads to poor interpolations when standard approaches are used; see Figure (1). To mitigate these effects, SnowMeLT incorporates recent advances that provide a more accurate treatment of the free surface. In the following, we discuss these effects and describe the approach presently used in SnowMeLT. A more in-depth discussion on this topic is given by Colagrossi et al. (2009). We also note that there are alternative approaches other than the one presented here. Notably, the use of additional "ghost" SPH-particles to account for the missing SPH-particles; see, e.g., Schechter and Bridson (2012).

To see the effect of missing SPH-particles, we consider a constant density field and write

$$\langle \rho \rangle_i \approx \rho_0 \sum_{j \in \Omega} \mathcal{W}_{ij} \, \Delta V_j \,, \tag{8}$$

where ρ_0 denotes the reference value of the density. In the interior where there is no deficiency of SPH-particles, Ω has support over the entire ball, $B_h(\|\mathbf{r} - \mathbf{r}'\|)$, and in light of the normalization condition, the RHS reproduces the correct value for the density; see appendix A. However, at the free surface $\Omega \neq B_h(\|\mathbf{r} - \mathbf{r}'\|)$, and the sum on the RHS is approximately the fraction Ω occupied by SPH-particles. As a result, Eq. (8) significantly underestimates the density and produces artificial density gradients near the surface that result in spurious pressure forces. To mitigate this effect in

SnowMeLT, the Shepard kernel is used to compute the density, viz.

$$< \rho(\mathbf{r}) >_i = \sum_{j \in \Omega} m_j \frac{\mathcal{W}_{ij}}{\Gamma_i}, \tag{9}$$

where

$$\Gamma_i = \sum_{j \in \Omega} \mathcal{W}_{ij} \, \Delta V_j \,, \tag{10}$$

is the Shepard normalization constant, and $< \cdot >$ is used to indicate its use as a correction. It is straightforward to verify that Eq. (9) now produces the correct density both in the interior and at the free surface.

The use of Eq. (9) for the density is important for getting the meltwater dynamics correct. However, it requires knowledge of the time evolution of the SPH-particle volumes. In SnowMeLT, the evolution of the SPH-paticle volumes are defined using the volumetric strain rate as,

$$\frac{d(\Delta V)}{dt} = \Delta V \, \nabla \cdot \mathbf{v} \,. \tag{11}$$

To evaluate this expression, a smoothed divergence is defined as

$$\langle \nabla \cdot \mathbf{v}(\mathbf{r}) \rangle = \int_\Omega \nabla' \cdot \mathbf{v}(\mathbf{r}') \mathcal{W}(\|\mathbf{r} - \mathbf{r}'\|, h) \, dV' \,. \tag{12}$$

To evaluate Eq. (12) in SPH, the gradient is first moved on to the kernel using

$$\langle \nabla \cdot \mathbf{v}(\mathbf{r}) \rangle = \int_\Omega \mathbf{v}(\mathbf{r}') \cdot \nabla \mathcal{W}(\|\mathbf{r} - \mathbf{r}'\|, h) \, dV' + \int_{d\Omega} \mathcal{W}(\|\mathbf{r} - \mathbf{r}'\|, h) \mathbf{v}(\mathbf{r}') \cdot \mathbf{n} \, dS' \,. \tag{13}$$

The volume integral can be evaluated readily, but surface integrals are not easily computed in SPH. In the interior, this difficulty can be avoided since $d\Omega$ coincides with the surface of $B_h(\|\mathbf{r} - \mathbf{r}'\|)$ where the kernel vanishes. However, at a free surface this is not the case, and dropping the surface term leads to larger errors, even for a constant field and vanishing smoothing length. A better choice

for the divergence can be formulated (and is commonly used) by first subtracting the identity

$$\mathbf{v}(\mathbf{r}) \cdot \left(\int_{\Omega} \nabla \mathcal{W}(\|\mathbf{r}-\mathbf{r}'\|, h) dV' + \int_{d\Omega} \mathcal{W}(\|\mathbf{r}-\mathbf{r}'\|, h) \cdot \mathbf{n}\, dS' \right) = 0\,, \tag{14}$$

and dropping the surface term to produce

$$\langle \nabla \cdot \mathbf{v}(\mathbf{r}) \rangle = \int_{\Omega} (\mathbf{v}(\mathbf{r}') - \mathbf{v}(\mathbf{r})) \cdot \nabla \mathcal{W}(\|\mathbf{r}-\mathbf{r}'\|, h)\, dV'\,. \tag{15}$$

This form of the divergence now produces the correct value for a constant field, and in the more general case converges at the free surface (Colagrossi et al. 2009), but it still has errors at finite resolution. To account for this, Grenier et al. (2009) proposed the normalized divergence,

$$< \nabla \cdot \mathbf{v} >_i = -\sum_{j \in \Omega} \mathbf{v}_{ij} \cdot \frac{\nabla \mathcal{W}_{ij}}{\Gamma_i} \Delta V_j\,, \tag{16}$$

which is the form adopted, presently. We also note that this form of the divergence is not specific to the velocity and can be used for any vector field. Similarly, the gradient of an SPH-field can be written as

$$\langle \nabla f \rangle_i = -\sum_{j \in \Omega} f_{ij} \nabla \mathcal{W}_{ij}\, \Delta V_j\,, \tag{17}$$

and corrected using

$$< \nabla f >_i = -\sum_{j \in \Omega} f_{ij} \frac{\nabla \mathcal{W}_{ij}}{\Gamma_i} \Delta V_j\,, \tag{18}$$

where f_{ij} denotes the difference $f_i - f_j$. To formulate the microphysics of SnowMeLT, an SPH approximation of the Laplacian is also required and is provided in appendix B.

3. Microphysics

Presently, the microphysics of SnowMeLT includes heat conduction, phase changes and latent heating, surface tension, contact forces, and viscous weakly-compressible flow. While this captures most of the important processes in the melting of ice hydrometeors, there are, of course, other

important processes, e.g., riming and sublimation, that are left for future work. In addition, some simplifying assumptions have been made. Perhaps the most significant assumption is that the distribution of unmelted ice is held fixed in space. This restriction leads to an unrealistic (and overly energetic) collapse of the snowflakes during the final stages of melting, making the results unreliable for meltwater fractions around 75% or larger. However, methods that allow for ice movement have already been formulated in SPH (e.g., Liu et al. (2014)), and ice movement will be included in the next version of SnowMeLT. In addition, to avoid the prohibitive cost of simulating the atmosphere with SPH, an analytic approximation for heat transfer from the environment is employed, here, based on steady-state transfer within the environment and the assumption of a uniform air temperature immediately surrounding the snowflake. In the following, the microphysics is discussed and developed in some detail.

a. Fluid Dynamics

The meltwater in SnowMeLT is represented as a weakly-compressible viscous fluid subject to surface tension and contact forces. The momentum equation takes the form

$$\rho \frac{d\mathbf{v}}{dt} = -\nabla p + \mathbf{f}_{\text{visc}} + \mathbf{f}_{\text{surf}}\,, \tag{19}$$

where $\mathbf{f}_{\text{visc}}$ and $\mathbf{f}_{\text{surf}}$ denote the viscosity and surface-tension force densities. The SPH formulation of this equation is the topic of the following sections. In addition to the momentum equation, an interface boundary condition between meltwater and ice is required and is discussed in the final section.

1) Weakly-Compressible Viscous Flow

To simulate a weakly-compressible fluid in SPH, the density and pressure of an SPH-particle is related by an equation-of-state (EOS). There are a few popular variants in the literature. In the current work, we use the Newton-Laplace EOS,

$$p_i = \left(< \rho >_i - \rho_0\right) c^2\,, \tag{20}$$

where ρ_0 and c denote the rest density and speed-of-sound in the fluid, respectively. In the above, the speed-of-sound determines how quickly the pressure responds to density variations in the fluid. It is impractical (and unfeasible) to simulate at the physical value of the speed-of-sound. Instead, c is chosen large enough to keep the density variations sufficiently small, typically $< 0.1\%$. Following Grenier et al. (2009), the pressure gradient in the momentum equation is derived from the Principle of Virtual Work for an isentropic fluid which states

$$\int_\Omega \nabla p \cdot \delta\mathbf{w}\, dV = -\int_\Omega p \nabla \cdot \delta\mathbf{w}\, dV\,, \tag{21}$$

where $\delta\mathbf{w}$ is the displacement due to the virtual work. To derive an SPH expression for Eq. (21) that includes a free surface correction, the divergence in Eq. (16) is used, from which it follows,

$$\sum_{i\in\Omega} \prec \nabla p \succ_i \cdot \delta\mathbf{w}_i \Delta V_i = -\sum_{i\in\Omega} \frac{p_i}{\Gamma_i} \sum_{j\in\Omega} (\delta\mathbf{w}_j - \delta\mathbf{w}_i) \cdot \nabla \mathcal{W}_{ij} \Delta V_j\,. \tag{22}$$

Re-arranging the sum on the RHS leads to

$$\prec \nabla p \succ_i = \sum_{j\in\Omega} \left(\frac{p_i}{\Gamma_i} + \frac{p_j}{\Gamma_j}\right) \nabla \mathcal{W}_{ij} \Delta V_j\,, \tag{23}$$

which is the form of the pressure gradient given in Grenier et al. (2009) and used in the current development. It preserves momentum and, importantly, the factors of Γ_i and Γ_j make a correction at the free surface.

Finally, the viscous force is derived from the viscosity equation of an incompressible fluid,

$$\mathbf{f}_{\text{visc}} = \nabla \cdot (\mu \nabla \mathbf{v})\,. \tag{24}$$

In appendix C, the derivation of a few variants of SPH viscosity terms are discussed, including the one proposed by Grenier et al. (2009), which is used in the present study. It takes the form

$$\prec \mathbf{f}_{\text{visc}} \succ_i = \sum_{j\in\Omega} \frac{8\mu_i\mu_j}{\mu_i + \mu_j} \left(\frac{1}{\Gamma_i} + \frac{1}{\Gamma_j}\right) \frac{\mathbf{v}_{ij}\cdot\mathbf{r}_{ij}}{r_{ij}^2} \nabla \mathcal{W}_{ij} \Delta V_j\,, \tag{25}$$

where $\mathbf{r}_{ij}$ denotes the difference $\mathbf{r}_i - \mathbf{r}_j$. This is a modified version of the viscosity proposed by Monaghan (2005) that provides a correction at the free surface through the factor $(\Gamma_i^{-1} + \Gamma_j^{-1})$. It preserves both angular and linear momentum, however, as discussed in appendix C, it does not converge to Eq (24), and in this sense, it is an artificial viscosity.

2) Surface Tension

The formulation of surface tension in SnowMeLT is derived from the continuum surface force (CSF) model. In this model, the surface tension is given by,

$$\mathbf{F}_{\text{surf}} = \sigma \kappa \hat{\mathbf{n}}, \tag{26}$$

where σ is the surface-tension force per unit length, κ is the curvature, and $\hat{\mathbf{n}}$ is the unit vector normal to the surface. To make this suitable for SPH, Brackbill et al. (1992) formulated Eq. (26) as a force density

$$\mathbf{f}_{\text{surf}}(\mathbf{r}) = \sigma \kappa \hat{\mathbf{n}} \delta\left(\hat{\mathbf{n}} \cdot (\mathbf{r} - \mathbf{r}_s)\right), \tag{27}$$

where $\mathbf{r}_s$ denotes the corresponding position on the surface. They introduced a color (characteristic) function,

$$c(\mathbf{r}) = \begin{cases} 1 & \text{in fluid 1}, \\ 0 & \text{in fluid 2}, \\ \frac{1}{2} & \text{at the interface}, \end{cases} \tag{28}$$

to define a smoothed surface normal,

$$\langle \mathbf{n}(\mathbf{r}) \rangle = \langle \nabla c(\mathbf{r}) \rangle \tag{29}$$

and delta function

$$\langle \delta\left(\hat{\mathbf{n}} \cdot (\mathbf{r} - \mathbf{r}_s)\right) \rangle = \| \langle \nabla c(\mathbf{r}) \rangle \|, \tag{30}$$

that are suitable for SPH and converge for any reasonable smoothing kernel. Using the SPH surface-normal, the curvature can be computed as

$$\langle \kappa(\mathbf{r}) \rangle = \langle -\nabla \cdot \hat{\mathbf{n}}(\mathbf{r}) \rangle \,, \tag{31}$$

which leads to

$$\langle \mathbf{f}_{\text{surf}}(\mathbf{r}) \rangle = \sigma \, \langle \kappa(\mathbf{r}) \rangle \, \langle \mathbf{n}(\mathbf{r}) \rangle \,, \tag{32}$$

for the SPH surface-tension force.

To implement Eq. (32) requires some care because of the use of normalized surface-normals. In particular, the surface normals become “small" with greater displacements from the surface and incur large (relative) numerical errors that when normalized lead to poor estimates of the curvature. To deal with this issue, we follow the approach of Morris (2000). In this approach, the smoothed color-function is defined in the usual way as,

$$\langle c \rangle_i = \sum_{j \in \Omega} c_j \mathcal{W}_{ij} \, \Delta V_j \,. \tag{33}$$

The surface normals are evaluated using Eq. (17) as

$$\langle \mathbf{n} \rangle_i = \sum_{j \in \Omega} \Big(\langle c \rangle_j - \langle c \rangle_i \Big) \nabla \mathcal{W}_{ij} \, \Delta V_j \,, \tag{34}$$

and the curvature is evaluated using Eq. (16) (without Shepard normalization) as,

$$\langle \nabla \cdot \hat{\mathbf{n}} \rangle_i = - \sum_{j \in \Omega} \langle \hat{\mathbf{n}} \rangle_{ij} \cdot \nabla \mathcal{W}_{ij} \, \Delta V_j \,, \tag{35}$$

where $\langle \hat{\mathbf{n}} \rangle_{ij}$ is the difference, $\langle \hat{\mathbf{n}} \rangle_i - \langle \hat{\mathbf{n}} \rangle_j$, of the unit normals $\langle \hat{\mathbf{n}} \rangle_i = \langle \mathbf{n} \rangle_i / \| \langle \mathbf{n} \rangle_i \|$. To avoid the errors associated with small normals, Morris (2000) proposed to include only the normals that

satisfy $\|\langle \mathbf{n} \rangle_i\| > 0.01/h$ in Eq. (35) and normalize the curvature by

$$\xi_i = \sum_{j \in \Omega_n} \mathcal{W}_{ij} \, \Delta V_j \,, \tag{36}$$

where Ω_n denotes the subset of normals in Ω that meet this criteria. The final form of the curvature is

$$\langle \kappa \rangle_i = \frac{\sum\limits_{j \in \Omega_n} \langle \hat{\mathbf{n}} \rangle_{ij} \cdot \nabla \mathcal{W}_{ij} \, \Delta V_j}{\xi_i} \,, \tag{37}$$

which can be combined with Eq. (34) to evaluate the SPH surface-tension force.

3) Contact Forces

While the surface tension just described can be used to simulate the dynamics of the air-meltwater interface, additional contact forces are required to reproduce the wetting behaviour of water on the ice surface. To achieve this we follow Trask et al. (2015) and impose Young's Equation by enforcing the equilibrium constraint,

$$\hat{\mathbf{n}}^{\mathrm{eq}} = \hat{\mathbf{n}}^t \sin\theta_{eq} + \hat{\mathbf{n}}^p \cos\theta_{eq} \,, \tag{38}$$

for the normals near to the ice/air/liquid boundary. In the above, $\hat{\mathbf{n}}^t$ and $\hat{\mathbf{n}}^p$ denote the components of the fluid normals tangent and perpendicular to the ice surface, and θ_{eq} denotes the equilibrium contact angle. Setting the fluid normals according to Eq. (38) ensures the SPH surface-tension will apply a force that continually works towards restoring the correct equilibrium behavior. To implement this approach, the ice-boundary normal, $\hat{\mathbf{n}}^p$, is computed using Eq. (34) with the sum being carried out over Ω_{ice}, where Ω_{ice} denotes the subset of SPH-particles in Ω that are ice. The component of the fluid normal tangent to the surface is then computed using

$$\left\langle \hat{\mathbf{n}}^t \right\rangle_i = \frac{\langle \hat{\mathbf{n}} \rangle_i - (\langle \hat{\mathbf{n}} \rangle_i \cdot \langle \hat{\mathbf{n}}^p \rangle_i) \langle \hat{\mathbf{n}}^p \rangle_i}{\| \langle \hat{\mathbf{n}} \rangle_i - (\langle \hat{\mathbf{n}} \rangle_i \cdot \langle \hat{\mathbf{n}}^p \rangle_i) \langle \hat{\mathbf{n}}^p \rangle_i \|} \,, \tag{39}$$

where $\langle \hat{\mathbf{n}} \rangle_i$ is the fluid normal evaluated using Eq. (34) over Ω_{wat}, the subset of SPH-particles in Ω that are water. Following Trask et al. (2015), we define a transition function

$$f_i = \begin{cases} \chi_i & \chi_i \geq 0\,, \\ 0 & \chi_i < 0\,, \end{cases} \tag{40}$$

in terms of a generalized distance,

$$\chi_i = 2\frac{\Gamma_i^{\text{wat}}}{\Gamma_i} - 1\,, \tag{41}$$

which provides a measure of how close a fluid SPH-particle is to the ice boundary. In Eq. (41), Γ_i^{wat} is computed using Eq. (10) over Ω_{wat}, and the ratio, $\Gamma_i^{\text{wat}}\Gamma_i^{-1}$, is used as a measure of the fraction of volume in Ω occupied by fluid SPH-particles. The function f_i takes values in the interval $[0, 1]$, and it is used to transition the normals across a displacement of roughly one smoothing length from the boundary. A new unit normal,

$$\langle \hat{\mathbf{n}}' \rangle_i = \frac{f_i \langle \hat{\mathbf{n}} \rangle_i - (1 - f_i) \langle \hat{\mathbf{n}}^{\text{eq}} \rangle_i}{\| f_i \langle \hat{\mathbf{n}} \rangle_i - (1 - f_i) \langle \hat{\mathbf{n}}^{\text{eq}} \rangle_i \|}\,, \tag{42}$$

is then defined, and Eq. (32) is replaced with

$$\langle \mathbf{f}_{\text{surf}} \rangle_i = \sigma \langle \kappa' \rangle_i \langle \hat{\mathbf{n}}' \rangle_i \| \langle \mathbf{n} \rangle_i \|\,, \tag{43}$$

where $\langle \kappa' \rangle_i$ is the curvature computed using $\langle \hat{\mathbf{n}}' \rangle_i$, and we have retained the surface delta function $\| \langle \mathbf{n} \rangle_i \|$.

4) Adhesion and the Boundary Between Water and Ice

As a snowflake melts, a boundary between meltwater and ice is formed, and boundary conditions must be enforced to prevent overlap of the two phases and to provide an appropriate slip condition for the flow of meltwater on the ice. Unlike the environmental air, the ice *is* simulated with SPH-particles, and these particles can be used as “dummy" boundary particles to enforce boundary conditions. In SnowMeLT, we follow the approach of Adami et al. (2012) which imposes a force

balance,

$$\frac{d\mathbf{v}_f}{dt} = -\frac{\nabla p}{\rho_f} + \mathbf{g} = \mathbf{a}_\mathrm{b}\,, \tag{44}$$

at the boundary, where here f denotes the fluid (meltwater), $\mathbf{g}$ the gravitational acceleration, and $\mathbf{a}_b$ the acceleration of the ice boundary. Integrating Eq. (44) along the line connecting a fluid and ice SPH-particle, we find

$$p_b = p_f + \rho_f(\mathbf{g} - \mathbf{a}_b)\cdot\mathbf{r}_{bf}\,, \tag{45}$$

which is used to extrapolate a value for the dummy pressure from nearby fluid SPH-particles. An SPH average is then formed in the usual way using the smoothing kernel to give

$$< p_b >_i = \frac{\sum\limits_{j\in\Omega_\mathrm{wat}} p_j \mathcal{W}_{ij}\,\Delta V_j + (\mathbf{g}-\mathbf{a}_b)\cdot\sum\limits_{j\in\Omega_\mathrm{wat}} \rho_j \mathbf{r}_{ij}\mathcal{W}_{ij}\,\Delta V_j}{\Gamma_i^\mathrm{wat}}\,. \tag{46}$$

Presently, in SnowMeLT there is neither gravity nor movement of the ice, and the above equation reduces to

$$< p_b >_i = \sum_{j\in\Omega_\mathrm{wat}} p_j \frac{\mathcal{W}_{ij}}{\Gamma_i^\mathrm{wat}}\,\Delta V_j\,. \tag{47}$$

In addition, the density and volume of dummy SPH-particles are determined using Eq. (20) as

$$\rho_b = \frac{< p_b > - \rho_0 c^2}{c^2} \quad \text{and} \quad dV_b = \frac{m_i}{\rho_b}\,, \tag{48}$$

where m_i is the mass of the fluid SPH-particle interacting with the dummy particle, and the subscript “b" is used to indicate a dummy quantity assigned to an ice SPH-particle for the purpose of enforcing a boundary condition. With Eq. (48), the pressure gradient near the boundary can be evaluated over Ω using dummy values for the ice SPH-particles.

A boundary condition for the viscosity is also required. Following Adami et al. (2012), an average velocity is computed using nearby fluid SPH-particles as

$$< \tilde{\mathbf{v}} >_i = \sum_{j \in \Omega_{\text{wat}}} \mathbf{v}_j \frac{\mathcal{W}_{ij}}{\Gamma_i^{\text{wat}}} \Delta V_j \,, \tag{49}$$

and the dummy velocity is set to

$$< \mathbf{v}_b >_i = 2\mathbf{v}_{\text{ice}} - < \tilde{\mathbf{v}} >_i \,, \tag{50}$$

where $\mathbf{v}_{\text{ice}}$ is the velocity of the ice boundary. Again, since the ice is held fixed this reduces to

$$< \mathbf{v}_b >_i = - < \tilde{\mathbf{v}} >_i \,. \tag{51}$$

In contrast to the pressure which keeps the ice and meltwater separated, the viscosity determines how much the meltwater “sticks" to the ice. To enforce a free-slip boundary condition, we set the dummy viscosity to zero, and to set a no-slip boundary condition, a relatively large viscosity is used. At this scale, the no-slip boundary layer is small compared to h, and as a result, a free-slip boundary condition is employed. However, we also need to account for adhesion between the meltwater and ice surface. To do this, the projection of the dummy velocity along the boundary normal perpendicular to the ice surface is used to replace Eq. (51) with

$$< \mathbf{v}_b >_i = - \left(< \mathbf{v} >_i \cdot \langle \hat{\mathbf{n}}^p \rangle \right) \langle \hat{\mathbf{n}}^p \rangle \,. \tag{52}$$

Using the projected velocities has the effect of “sticking" the meltwater along the direction normal to the ice surface while allowing it to flow freely across it. The value of the dynamic viscosity of dummy ice SPH-particles then plays the role of an adhesion strength parameter. In this work, we set it equal to the fluid viscosity, which gives reasonable results.

b. Thermodynamics

The thermodynamics of SnowMeLT includes heat conduction, phase changes and associated latent heating. Evaporation of meltwater is not simulated in the present formulation of SnowMeLT.

If the environment of the hydrometeor is subsaturated, evaporation could consume sensible heat and significantly reduce the rate of melting, but in remote sensing applications, for example, the melt fraction and geometry of the particle are the most critical factors for calculating single-scattering properties, and 1D thermodynamic models have been used to separately calculate the melt fractions of snowflakes of different masses; see, e.g., Olson et al. (2001) and Liao et al. (2009). Evaporation and other microphysical processes will be considered in future updates of SnowMeLT.

The heat conduction is implemented following the approach of Cleary and Monaghan (1999) which is derived from the incompressible heat equation

$$\frac{dU}{dt} = \frac{1}{\rho}\nabla \cdot (\kappa \nabla T) \,, \tag{53}$$

where viscous dissipation effects are assumed to be negligible. In the above, U and κ denote the energy density [J/g] and conductivity [W/(m-°C)], respectively. To convert Eq. (53) to an SPH-equation, Cleary and Monaghan (1999) used a Taylor Series approximation of the Laplacian (see appendix B) and enforced heat-flux continuity across material interfaces to derive

$$\left\langle \frac{dT}{dt} \right\rangle_i = \frac{4}{c_{v,i}\rho_i} \sum_{j \in \Omega} \frac{\kappa_i \kappa_j}{\kappa_i + \kappa_j} \left(T_i - T_j\right) F_{ij} \, \Delta V_j, \tag{54}$$

where the relationship between temperature and energy density is taken as $U = c_v T$ with $c_{v,i}$ denoting the specific heat. Important for this work, they showed through a series of numerical experiments that Eq. (54) can accurately simulate discontinuities in the conductivity of up to three orders of magnitude which is sufficient for simulations with air, ice, and water.

The evaluation of Eq. (54) is straightforward except at the boundary between the hydrometeor and surrounding environment. To simulate the transfer of heat from the surrounding environment, a method is required to transfer heat across the hydrometeor-atmosphere interface that includes a far-field temperature boundary condition and does not require simulating air SPH-particles explicitly. To do this, we make the assumption that the surrounding air temperature near to the surface, T_{air}, is uniform. According to Eq. (54), the contribution from air is

$$\left\langle \frac{dT^{\text{air}}}{dt} \right\rangle_i = \frac{4}{c_{v,i}\rho_i} \frac{\kappa_i \kappa_{\text{air}}}{\kappa_i + \kappa_{\text{air}}} \left(T_i - T_{\text{air}}\right) \sum_{j \in \Omega_{\text{air}}} F_{ij} \, \Delta V_j \,. \tag{55}$$

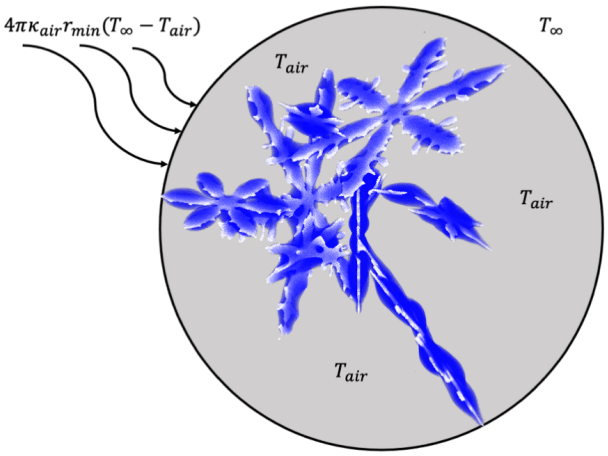

FIG. 2. Depiction of the heat transfer from the surrounding environment using a uniform air temperature, T_{air}, within a minimally circumscribing sphere and a radially-symmetric steady-state solution as a boundary condition with a far-field temperature, T_∞.

The sum on the RHS cannot be evaluated explicitly without simulating air SPH-particles, but it can be evaluated indirectly which follows from the fact that $\langle F(\mathbf{r})\rangle$ can be determined analytically over Ω; see, Appendix (5). We note that this sum is a purely geometric term which can be thought of as a shape factor that takes into account the amount of nearby surrounding air. In areas where the surface is more exposed, this term becomes larger causing extremities to melt faster. The heat conduction at the boundary is then computed by evaluating Eq. (54) and adding the result of Eq. (55). Importantly, Eq. (55) vanishes in the interior and can safely be added regardless of whether the SPH-particle being updated lies on the surface or not. This avoids the need to identify surface SPH-particles which is difficult and error prone. To impose a far-field temperature boundary condition, the melting snowflake is first enclosed by a minimally circumscribing sphere; see Figure (2). The temperature field outside the sphere is derived as a radially-symmetric, analytical solution of the steady-state heat equation, with a temperature T_{air} on the circumscribing sphere and a temperature T_∞ at some large radial distance serving as boundary conditions; see Mason (1956). Continuity is imposed between the "exterior" heat equation solution and the "interior" solution from SPH (with a uniform near-surface air temperature, T_{air}), by setting the radial transfer of thermal power from both solutions equal at the radius of the circumscribing sphere; see Appendix (5).

Lastly, to take into account latent heat, we use an internal (thermal) energy parameter that is initialized to zero. For ice SPH-particles, the internal energy is updated using the energy-density form of Eq. (54). Once the internal energy of an SPH-particle surpasses $L_f\times$ SPH-particle mass, where L_f is the latent heat of fusion, the ice SPH-particle becomes a fluid SPH-particle, and its temperature is updated according to Eq. (54).

4. Numerical Examples

To test SnowMeLT, a series of numerical experiments are conducted using synthetic snowflakes available from the NASA OpenSSP database. The database includes pristine dendritic crystals of different shapes generated using the algorithm of Gravner and Griffeath (2009), as well as aggregates created using a randomized collection process (Kuo et al. 2016). In the present study, snowflakes with maximum dimensions up to $\sim$ 1 cm are melted; Larger snowflakes will require the use of hardware accelerators which are not currently implemented in SnowMeLT. Since the snowflakes in the database are already defined on a regular grid, it is straightforward to ingest them into SnowMeLT. Here, the initial grid spacing (dx) and SPH-particle mass are set to 15 μm and $\rho_{\text{ice}}\Delta V = 3.1x10^{-9}$ g. The value of the simulation parameters used in all of the examples are listed in Table (1), and with exception of the speed-of-sound, gravity, and viscosity, are set to their physical values. The speed-of-sound was tuned to keep deviations from the rest density at or below $\sim 0.1\%$, and the fluid viscosity was chosen large enough to maintain numerical stability. The simulation is advanced using the kick-drift-kick time integration scheme described in Appendix (5).

In section a, simple examples of the deformation of a cube of water are presented as a check of the surface tension and contact forces. In section b, ice spheres are melted using both SnowMeLT and a multi-shell numerical method to check the consistency of the evolving internal temperature and total melt time of the melting spheres. In section c, numerical experiments to determine the effect of the thermal vs. fluid timestep on a small pristine snowflake are examined, and in section d, the application of SnowMeLT to a set of aggregate snowflakes is presented and discussed.

a. Deformation of a Cube of Water

To test the surface tension in SnowMeLT, a cube of water is allowed to deform into a spherical water drop. The cube is composed of a collection of $\sim$132-thousand SPH-particles with a volume

Parameter	Value	Units
dx (rest distance)	15	μm
h (smoothing length)	45	μm
θ (contact angle)	10	$^\circ$
c_{sound}	2500	cm/s
κ_{water}	0.556	W/(m-°C)
κ_{ice}	2.22	W/(m-°C)
κ_{air}	0.0244	W/(m-°C)
$c_{\text{v,water}}$	4.22	J/(g-°C)
$c_{\text{v,ice}}$	2.05	J/(g-°C)
σ	0.072	N/m
μ_{ice}	0.4	g /(cm-s)
μ_{wat}	0.4	g /(cm-s)
$\mathbf{g}$	0	cm/s^2
T_∞	1.5	°C
L_f	334	J/g
ρ_{ice}	0.917	g/cm^3
ρ_{wat}	1.0	g/cm^3

TABLE 1. List of the simulation parameters used in this work.

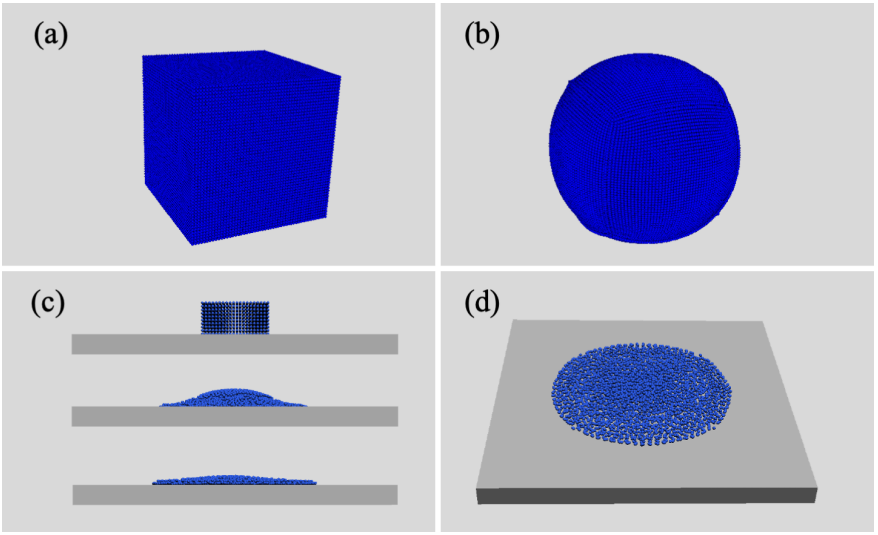

FIG. 3. An initial cube of water, (a), deforms into a spherical drop, (b), and a cube of water deforms into a sessile drop on an ice slab, (c) and (d). In (c), the initial state (top) is shown along with the final states for $\theta_{eq} = 30^\circ$ (middle) and $\theta_{eq} = 10^\circ$ (bottom). In (d), a top-view of the final state for $\theta_{eq} = 10^\circ$ is also shown.

equal to ~ 0.75 mm^3. Similarly, to test the contact forces, a cube of water composed of ~36-thousand SPH-particles is placed on top of a sheet of ice and allowed to deform for the cases

diameter [mm]	total time SPH [s]	total time multi-shell [s]
0.25	47.8	44.9
0.50	186.5	179.9
1.00	733.6	720.0

TABLE 2. Total time to completely melt frozen spheres using SPH and the multi-shell model.

$\theta_{eq} = 30°$ and $\theta_{eq} = 10°$, which is roughly the range of observed contact angles. The results of both tests are shown in Figure (3). Note that the water cube evolves into a nearly perfect water sphere, due to the effects of surface tension, and the sessile drops on the ice slabs exhibit contact angles close to the prescribed values of θ_{eq}, as seen in the figure.

b. Melting Frozen Spheres

To provide a check of the thermal processes, pure ice spheres are melted with SnowMeLT and a discrete, concentric shell model, and compared. The shell model employs finite-differencing of properties between adjacent shells to determine the heat flux between shells, and then raises the temperature of a given shell once the internal energy exceeds the total required to melt the entire mass of ice in that shell. This alternative approach is a generalization of the "enthalpy method" to spherically-symmetric ice particles; see Alexiades and Solomon (1993), who described a one-dimensional application. Sensible heat fluxes from the environment are specified using steady air temperature solutions of the heat equation, similar to the way heat fluxes are specified using Eq. (54). Although the shell model is only approximate and does not represent the flow of meltwater, it provides a reasonable check of the very detailed SnowMeLT simulations for ice spheres.

Ice spheres with diameters of 0.25 mm, 0.5 mm, and 1.00 mm are melted using SnowMeLT and the shell model. The times of complete ice sphere melting from both models differ between about 2% and 6% with a smaller percentages associated with larger radii; see Table (2). The time-progression of internal temperatures also show good agreement, and in Figure (4), the results for the 1.00 mm diameter sphere are presented. The undulations of the temperature contours in the multi-shell simulation are due to the constant temperature within the outermost icy shell as the ice melts, followed by the rapid increase of temperature in that shell as the temperature comes to a new quasi-equilibrium after the ice melts completely.

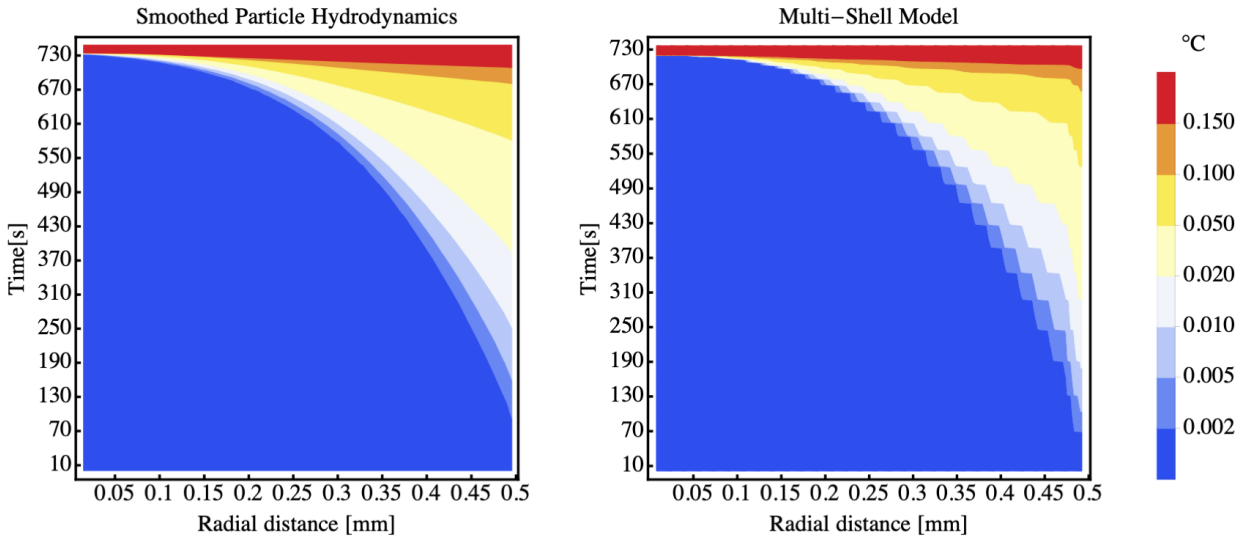

FIG. 4. Thermal profiles of the internal temperatures for the 1 mm diameter frozen sphere using SnowMeLT (left) and the multi-shell model (right).

c. Varying the Thermal Timestep of a Dendritic Pristine Snowflake

Using the simulation parameters in Table (1) to determine the constraints given in Appendix (5) leads to a fluid timestep about three orders of magnitude smaller than the timestep required for thermal processes. This is not surprising — the meltwater response to surface-tension forces at this scale and temperature occur much more rapidly than the internal energy/melting response to heat transfer. From a computational perspective, incrementing the simulation at the fluid timestep would require on the order of 10^{10} steps for the largest snowflakes listed in Table (3). This is not feasible even on large supercomputers. It is therefore necessary to increase the thermal timestep as much as possible to reduce the computational burden (the thermal timestep dictates the physical simulation time), while incrementing the fluid changes at the much smaller timestep. This dual timestepping is possible because of the rapid response of the meltwater to structural changes in the ice.

To determine an appropriate increase, a pristine snowflake with a diameter of 1.3 mm was melted with a thermal timestep 125, 250, 500, 1000, and 2000 times larger than the fluid timestep. The images of the crystal at different melt stages are shown in Figure (5). For the case of the largest scale factor there is limited pooling in the snowflake crevices and a relatively thick layer of meltwater coating the arms. As the scale factor decreases, the meltwater has more time to

name	diameter [mm]	total mass [mg]	# SPH-particles	time-steps	total time [s]
01_0013_013	10.4	6.872	2,220,518	15,072,000	929
01_0012_022	10.5	6.429	2,077,299	13,984,000	866
01_0033_017	8.51	4.342	1,482,991	11,008,000	686
01_0011_010	7.83	3.692	1,192,808	10,432,000	650
01_0030_005	6.10	2.251	727,289	8,576,000	530
01_0033_008	6.11	2.111	682,020	7,904,000	490
01_0032_007	5.35	1.490	481,504	6,624,000	411
01_0030_003	4.61	0.856	276,650	4,768,000	313
01_0014_003	3.21	0.495	159,957	3,840,000	238
01_0074_010	2.80	0.367	118,534	3,232,000	200
01_0072_013	2.08	0.184	59,600	2,144,000	133

TABLE 3. A list of the properties for the 11 snowflakes melted with SnowMeLT. The columns from left-to-right correspond to the NASA openSSP database name, diameter of the (initial) minimally circumscribing sphere, total mass, number of SPH-particles simulated, and total time-steps and time to melt.

move along the surface of the crystal in a given thermal timestep, and as expected from surface tension considerations, we see increased pooling towards the center of the flake and more exposed extremities. From scaling factors of 500 to 125, we see very little change, indicating the former is a reasonable choice for increasing the thermal timestep — at least for this particular snowflake. As a result of this test, all of the aggregate snowflakes presented in this study are melted using a thermal timestep equal to the fluid timestep scaled by a factor of 500. In spite of the increased thermal timestep, numerical simulations of the largest snowflake require millions of timesteps and run continuously for about two months using $\sim$ 800 compute cores on the NASA Discover supercomputer.

d. Melting Aggregate Snowflakes

As a demonstration of the general applicability of SnowMeLT, a set of eleven aggregate snowflakes are melted, ranging in size from 2-10.5 mm in maximum dimension. In Table (3), we list the corresponding name, size, mass, number of SPH-particles used, total number of timesteps required, as well as the total time simulated. The aggregates are composed of different numbers of pristine dendritic crystals, with 22 crystals being the largest number. The snowflake with the largest mass is represented by 2,220,518 SPH-particles and requires over 15 million timesteps to com-

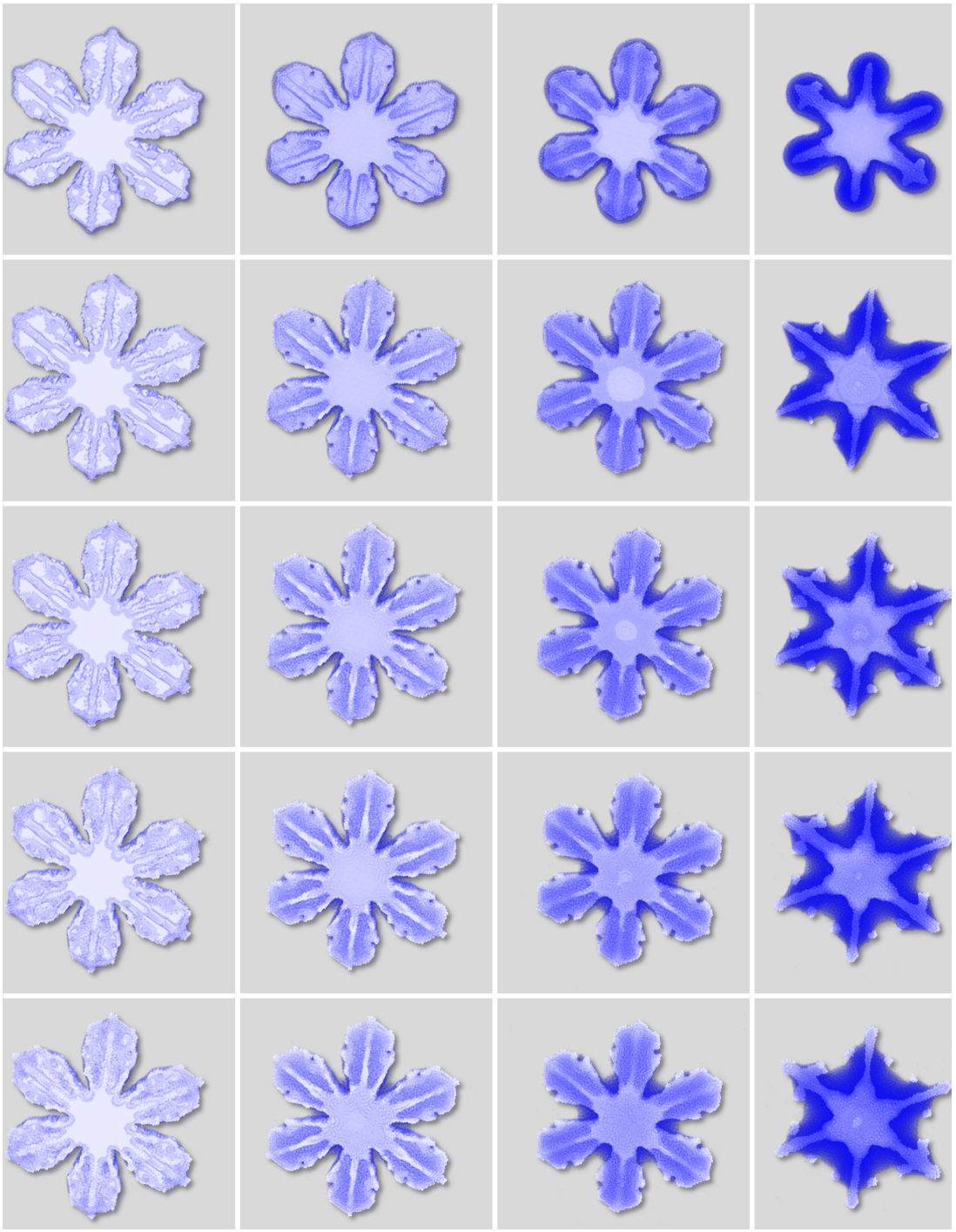

FIG. 5. Snapshots of a pristine snowflake with the thermal timestep scaled by 2000, 1000, 500, 250, and 125 (top-to-bottom) at melt stages of 20%, 40%, 60%, and 80% (left-to-right).

pletely melt. Images of the aggregates at different stages of melting are presented in Figures (6-8) at mass melt fractions of 30%, 50%,70%,90% and 100% (top-to-bottom).

From the figures, it is evident that at 30% melted the snowflakes are lightly coated with a layer of meltwater and exhibit some slight pooling of liquid in the crevices between ice structures. At 50% melted, more collecting and pooling of meltwater in the cervices is seen. Focusing in on the individual crystals that make up the aggregates, two distinguishing behavioral types are observed: Crystals with fine-scale filaments and ice "spikes" protruding from the arms and crystals without these structures . In the former type, meltwater tends to be distributed more on the arms, where it gets held up by surface tension in the crevices between the fine-scale structures. In crystals without fine-scale structures, the water is able to flow more easily towards the crystal centers, leading to the formation of a central water drop; see for example, Figure (8), column two). These behaviors were previously observed in laboratory grown and melted dendritic arms and plates by Oraltay and Hallett (2005). At 50% melted, water collecting in the junctions between the individual crystals can also be seen. At 70% melted, elongated water drops cover the crystal arms, large water drops bulge over the centers of the crystals, and crevices and gaps between the crystals are largely filled. At 90% melted, the component crystals are mostly engulfed by meltwater, though the aggregates still generally retain a coarse ice frame. At this stage, the effects of keeping the ice SPH-particles fixed in space become evident. For example, in the first column of Figure (7), we see the presence of small, detached ice chunks that would have otherwise been drawn inwards. The artificial bridges of water between the main ice structures and these small ice chunks create large surface tension forces that “snap" the liquid abruptly once a particular ice chunk fully melts. This energetic release leads to an eruption of minute water droplets, as seen in the figure. As a result, the final collapse of the aggregates (meltwater fractions $\gtrsim 75\%$) tends to be unrealistic for the larger aggregates. For the aggregates of crystals with more plate-like arms, this phenomenon does not occur, and we see a more realistic collapse of the aggregate into a water droplet; see Figure (8), column three.

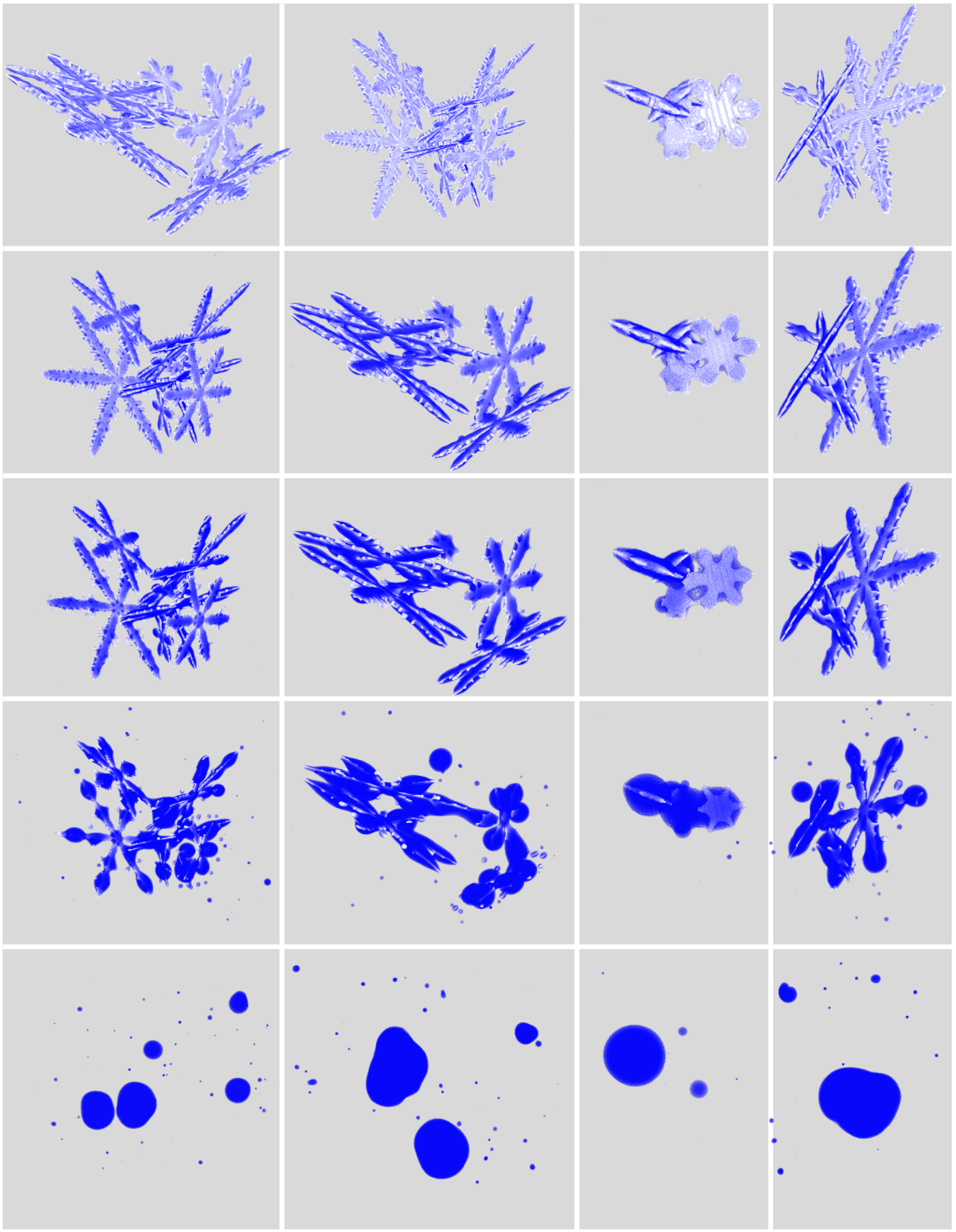

FIG. 6. Snapshots of the snowflakes 1-4 listed in Table (3) at 30%, 50%, 70%, 90%, and 100% melted (top-to-bottom).

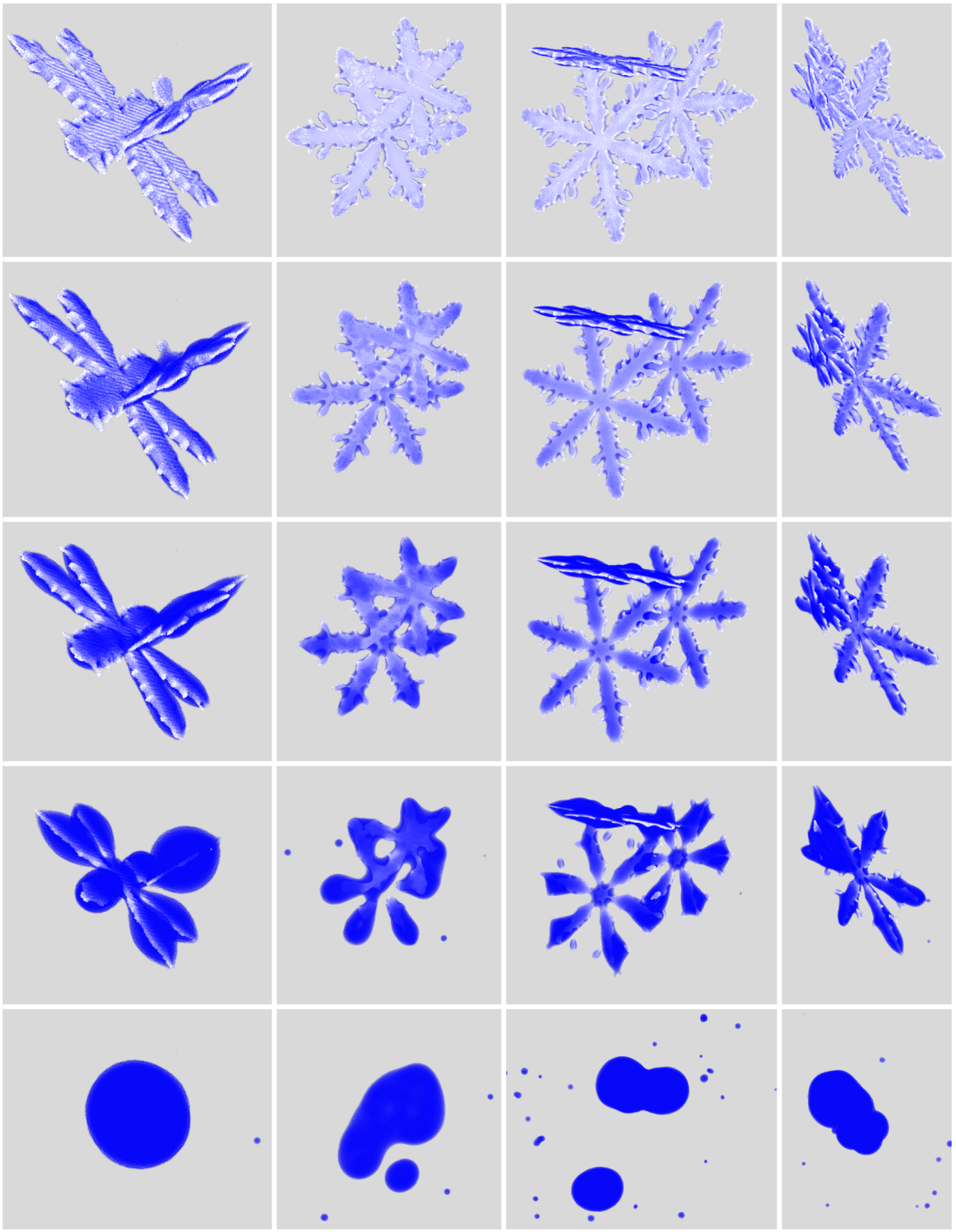

FIG. 7. Snapshots of the snowflakes 5-8 listed in Table (3) at 30%, 50%, 70%, 90%, and 100% melted (top-to-bottom).

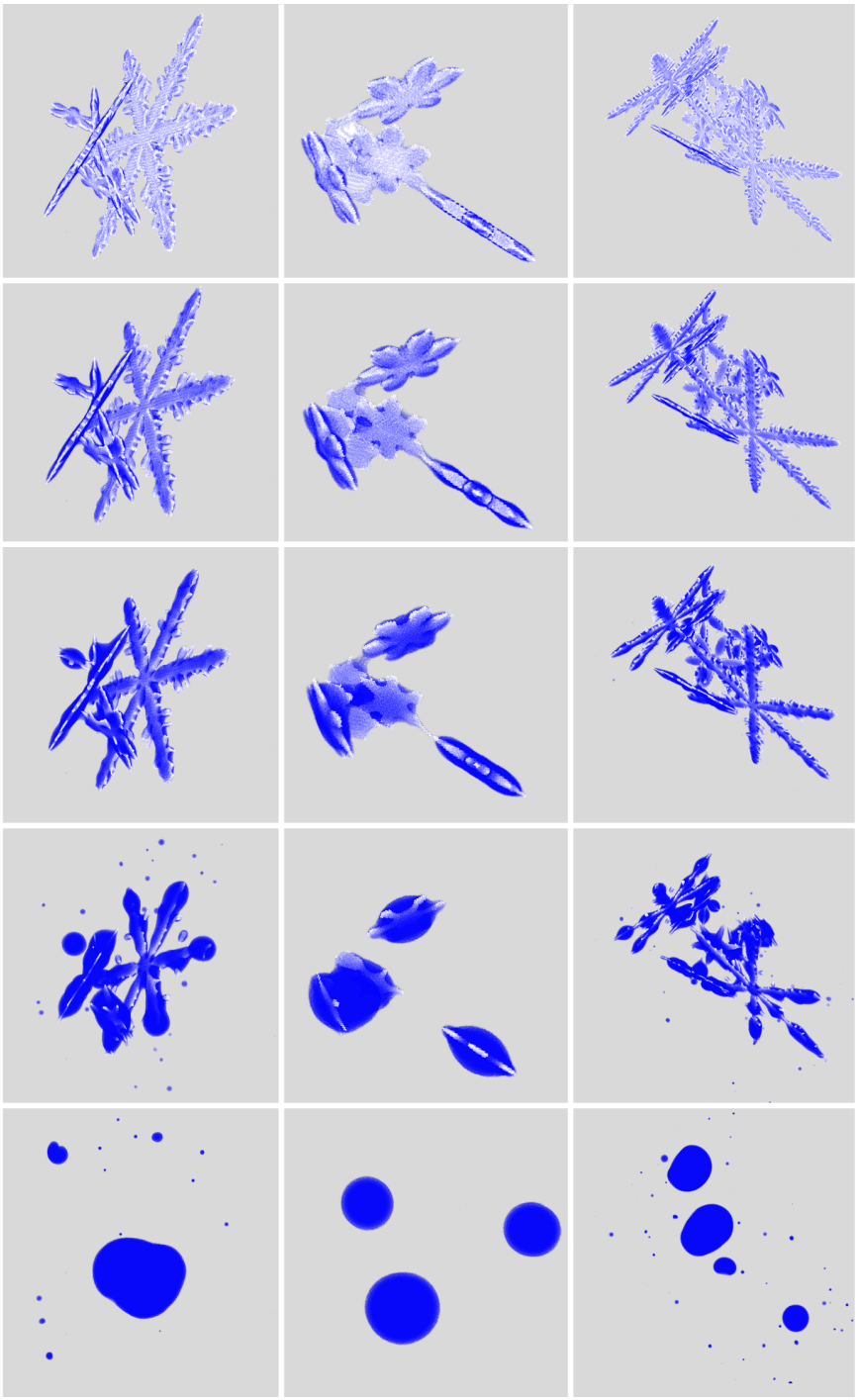

FIG. 8. Snapshots of the snowflakes 9-11 listed in Table (3) at 30%, 50%, 70%, 90%, and 100% melted (top-to-bottom).

5. Concluding Remarks

An SPH approach for computationally melting ice-phase hydrometeors is presented along with applications to a variety of synthetic snowflakes retrieved from the NASA OpenSSP database. The microphysics of the approach is derived directly from continuum physics conservation equations with the exception of the adhesive force between water and ice, and recent advances in free-surface flows are employed that are important for simulating the movement of thin layers of meltwater. To manage the computational cost, controlled approximations and some simplifications are used: One approximation is that the thermal (physical) timestep is effectively increased relative to the fluid dynamics timestep, because the rate of meltwater flow and other processes are relatively fast and respond to ice geometry changes very quickly. The much shorter fluid timestep, consistent with the Courant-Friedrichs-Lewy and other stability citeria given in appendix E, can therefore be used to increment meltwater flow while maintaining the integrity of the simulation. Here, the thermal timestep inflation is chosen based on trials of the melting of a single pristine snowflake, and a more thorough study of timestepping effects should be conducted for a variety of snowflake shapes and sizes. This more thorough study will become more practical with the use of hardware accelerators.

Another modification is that the heat exchange with the environment is approximated assuming a steady-state transfer of sensible heat to a sphere enclosing the snowflake. The air temperature within the sphere and near the snowflake's surface is assumed to be homogeneously-distributed. Although the air temperature is assumed to be the same near the surface of the snowflake, the heat transfer is distributed heterogeneously across the surface of the snowflake according to the local air exposure, surface temperature, and water phase, and therefore the boundary specification is still expected to reasonably capture the ambient heat transfer. Finally, the ice is not allowed to move, and in most but not all cases this leads to a significant distortion of the final collapse of the snowflake into a water drop. What results is an ice morphology in the latter stages of melting that is unrealistic, but there exist SPH approaches that can be used to remove this constraint (e.g., Liu et al. (2014)), and these approaches will be investigated in the next generation of SnowMeLT.

For remote sensing applications, a substantial number of melting hydrometeors and their scattering properties will be required to define the average properties of hydrometeors of a given mass, meltwater fraction, habit, etc. Perhaps the most significant obstacle to producing a large collection of melted hydrometeors with the SPH approach is the computational cost. The current

implementation requires about two months on 800 compute cores to melt the largest aggregate snowflake described here; see Table (3). Snowflakes at least two to three times larger can be found in stratiform rain systems, and to melt them will require a boost in computing power. It is already well established that SPH performs well on Graphical Processing Units (GPUs), and it is anticipated that they will be able to provide this boost. With the large number of available GPU resources, both in the cloud and at supercomputing centers, it should be possible to generate a diverse collection of partially-melted synthetic snowflakes in the near future for remote sensing applications.

Acknowledgments. We want to thank Tom Clune and Benjamin Johnson for useful discussions. We also want to thank K. Iwasaki for providing his code for preliminary test. This work is supported by NASA ROSES NNH18ZDA001N-PMMST.

APPENDIX A

The Wendland C^2 Kernel

In this work, the Wendland C^2 kernel,

$$\mathcal{W}_{\rm wend}(\|\mathbf{r}\|,h) = \frac{21}{2\pi h^3}\begin{cases} (1-r/h)^4\,(1+4r/h) & 0\le r<h, \\ 0 & \text{otherwise}, \end{cases} \tag{A1}$$

with normalization,

$$\int \mathcal{W}_{\rm wend}(\|\mathbf{r}\|,h)\,dV = 1\,, \tag{A2}$$

is used. The gradient of this kernel is given by

$$\nabla\mathcal{W}_{\rm wend}(\|\mathbf{r}\|,h) = -\frac{210}{\pi h^5}\begin{cases} (1-r/h)^3\,\mathbf{r} & 0\le r<h \\ 0 & \text{otherwise} \end{cases}\,. \tag{A3}$$

Writing the kernel in terms of the relative position between SPH-particles $\mathbf{r} = \mathbf{r}' - \mathbf{r}''$, the gradient with respect to individual coordinates is given by

$$\nabla'\mathcal{W}(\|\mathbf{r}'-\mathbf{r}''\|,h) = \nabla\mathcal{W}(\|\mathbf{r}\|,h) \quad \text{and} \quad \nabla''\mathcal{W}(\|\mathbf{r}'-\mathbf{r}''\|,h) = -\nabla'\mathcal{W}(\|\mathbf{r}'-\mathbf{r}''\|,h)\,. \tag{A4}$$

The integral of the gradient over $\Omega = B_h\,(|\mathbf{r}-\mathbf{r}'|)$,

$$\int_\Omega \nabla\mathcal{W}(\|\mathbf{r}-\mathbf{r}'\|,h)\,dV' = \int_{d\Omega} \mathcal{W}(\|\mathbf{r}-\mathbf{r}'\|,h)\hat{\mathbf{n}}' = 0\,, \tag{A5}$$

vanishes since $d\Omega$ coincides with the surface of the ball where the kernel support vanishes. It is also common to write the kernel gradient in the form (e.g., Cleary and Monaghan (1999))

$$\nabla \mathcal{W}(\|\mathbf{r}\|, h) = F(r)\,\mathbf{r}\,, \tag{A6}$$

with

$$F(r) = -\frac{210}{\pi h^5}\begin{cases} (1-r/h)^3 & 0 \le r < h\,, \\ 0 & \text{otherwise}\,. \end{cases} \tag{A7}$$

For the Wendland C^2 kernel,

$$\int_\Omega F(r)\,dV = -\frac{14}{h^2}\,, \tag{A8}$$

which is used to compute the environmental heat transfer, c.f. Eq. (D5).

APPENDIX B

Smoothed Approximation of the Laplacian

To derive an SPH approximation of the Laplacian, a Taylor Series expansion is applied to a generic field as

$$f(\mathbf{r}') - f(\mathbf{r}) = \nabla f(\mathbf{r}) \cdot (\mathbf{r}' - \mathbf{r}) + \sum_{i,j} \frac{1}{2}\frac{\partial^2 f(\mathbf{r})}{\partial r_i \partial r_j}(\mathbf{r}' - \mathbf{r})_i (\mathbf{r}' - \mathbf{r})_j + O\left(|\mathbf{r}' - \mathbf{r}|^3\right)\,. \tag{B1}$$

Multiplying this by the term,

$$\frac{(\mathbf{r} - \mathbf{r}') \cdot \nabla \mathcal{W}(\|\mathbf{r} - \mathbf{r}'\|)}{\|\mathbf{r} - \mathbf{r}'\|^2}\,, \tag{B2}$$

dropping the higher order terms, and integrating over $\mathbf{r}'$ produces

$$\int_\Omega (f(\mathbf{r}') - f(\mathbf{r})) \frac{(\mathbf{r}-\mathbf{r}')\cdot\nabla\mathcal{W}(\|\mathbf{r}-\mathbf{r}'\|)}{\|\mathbf{r}-\mathbf{r}'\|^2}\, dV' = \tag{B3}$$

$$\nabla f(\mathbf{r}) \cdot \int_\Omega (\mathbf{r}'-\mathbf{r}) \frac{(\mathbf{r}-\mathbf{r}')\cdot\nabla\mathcal{W}(\|\mathbf{r}-\mathbf{r}'\|)}{\|\mathbf{r}-\mathbf{r}'\|^2}\, dV' \tag{B4}$$

$$+ \sum_{i,j} \frac{1}{2} \frac{\partial^2 f(\mathbf{r})}{\partial r_i \partial r_j} \int_\Omega (\mathbf{r}'-\mathbf{r})_i (\mathbf{r}'-\mathbf{r})_j \frac{(\mathbf{r}-\mathbf{r}')\cdot\nabla\mathcal{W}(\|\mathbf{r}-\mathbf{r}'\|)}{\|\mathbf{r}-\mathbf{r}'\|^2}\, dV' \,. \tag{B5}$$

By noticing the first term on the RHS is odd, we immediately see it vanishes. Similarly, the off-diagonal elements of the second order term vanish leaving only the terms

$$\sum_i \frac{1}{2} \frac{\partial^2 f(\mathbf{r})}{\partial r_i^2} \int_\Omega (\mathbf{r}'-\mathbf{r})_i^2 \frac{(\mathbf{r}-\mathbf{r}')\cdot\nabla\mathcal{W}(\|\mathbf{r}-\mathbf{r}'\|)}{\|\mathbf{r}-\mathbf{r}'\|^2}\, dV' \,. \tag{B6}$$

To evaluate the integrals, we take $\mathbf{r}'' = \mathbf{r} - \mathbf{r}'$ and look at the z'' term

$$\int_\Omega z''^2 \frac{\mathbf{r}''\cdot\nabla\mathcal{W}(\|\mathbf{r}''\|}{\|\mathbf{r}''\|^2}\, dV'' = \int_{d\Omega} z''^2 \frac{\mathcal{W}(\|\mathbf{r}''\|)}{\|\mathbf{r}''\|^2} \mathbf{r}''\cdot\hat{\mathbf{n}}\, dS'' - \int \nabla\cdot\left(\frac{z''^2}{\|\mathbf{r}''\|^2}\mathbf{r}''\right)\mathcal{W}(\|\mathbf{r}''\|) dV'' \,. \tag{B7}$$

Since $\mathcal{W}(\|\mathbf{r}''\|) = 0$ on $d\Omega$ the surface integral vanishes (though, not at a free surface), and the remaining term evaluates to

$$\int \nabla\cdot\left(\frac{z''^2}{\|\mathbf{r}''\|^2}\mathbf{r}''\right)\mathcal{W}(\|\mathbf{r}''\|) dV'' = 1 \,. \tag{B8}$$

The same follows for the x and y terms, and we find

$$\left\langle \nabla^2 f(\mathbf{r}) \right\rangle = 2 \int_\Omega (f(\mathbf{r}) - f(\mathbf{r}')) \frac{(\mathbf{r}-\mathbf{r}')\cdot\nabla\mathcal{W}(\|\mathbf{r}-\mathbf{r}'\|)}{\|\mathbf{r}-\mathbf{r}'\|^2}\, dV' \,, \tag{B9}$$

as a smoothed approximation for the Laplacian and

$$\left\langle \nabla^2 f \right\rangle_i = 2 \sum_{j\in\Omega} \left(f_i - f_j\right) \frac{\mathbf{r}_{ij}\cdot\nabla\mathcal{W}_{ij}}{r_{ij}^2} \Delta V_j \,, \tag{B10}$$

for the discrete form.

APPENDIX C

On the Formulation of Viscosity in SnowMeLT

The viscosity for an incompressible fluid is given by the vector Laplacian equation

$$\mathbf{f}_{\text{visc}} = \nabla \cdot (\mu \nabla \mathbf{v}) \,, \tag{C1}$$

which in Cartesian coordinates reduces to a regular Laplacian for each component. We consider the x-component and expand the product to get

$$\mathbf{f}_{\text{visc},x} = \nabla \cdot (\mu \nabla \mathbf{v}_x) = \frac{1}{2}\left(\nabla^2(\mu \mathbf{v}_x) - \mathbf{v}_x \nabla^2 \mu + \mu \nabla^2 \mathbf{v}_x\right) \,. \tag{C2}$$

Using Eq. (B10) and collecting terms produces

$$\left\langle \mathbf{f}_{\text{visc},x} \right\rangle_i = \sum_{j \in \Omega} \left(\mu_i + \mu_j\right) \mathbf{v}_{x,ij} \frac{\mathbf{r}_{ij} \cdot \nabla \mathcal{W}_{ij}}{r_{ij}^2} \Delta V_j \,, \tag{C3}$$

from which it follows

$$\langle \mathbf{f}_{\text{visc}} \rangle_i = \sum_{j \in \Omega} \left(\mu_i + \mu_j\right) \mathbf{v}_{ij} \frac{\mathbf{r}_{ij} \cdot \nabla \mathcal{W}_{ij}}{r_{ij}^2} \Delta V_j \,. \tag{C4}$$

To ensure flux continuity across discontinuities in the viscosity, Cleary and Monaghan (1999) showed the above formula should be replaced with

$$\langle \mathbf{f}_{\text{visc}} \rangle_i = \sum_{j \in \Omega} \frac{4\mu_i \mu_j}{\mu_i + \mu_j} \mathbf{v}_{ij} \frac{\mathbf{r}_{ij} \cdot \nabla \mathcal{W}_{ij}}{r_{ij}^2} \Delta V_j \,. \tag{C5}$$

To take into account the free surface Grenier et al. (2009) modified Eq. (C5) as

$$\prec \mathbf{f}_{\text{visc}} \succ_i = \sum_{j \in \Omega} \frac{2\mu_i \mu_j}{\mu_i + \mu_j} \left(\frac{1}{\Gamma_i} + \frac{1}{\Gamma_j}\right) \mathbf{v}_{ij} \frac{\mathbf{r}_{ij} \cdot \nabla \mathcal{W}_{ij}}{r_{ij}^2} \Delta V_j \,. \tag{C6}$$

In the interior where Γ_i and Γ_i are ~ 1, it is easy to verify Eq. (C6) reproduces Eq. (C5), and therefore the modification only provides a correction at a free surface. This form of the viscosity

preserve linear momentum but not angular momentum. If we decompose Eq. (C5) as

$$\langle \mathbf{f}_{\rm visc} \rangle_i = \sum_{j\in\Omega} \frac{4\mu_i\mu_j}{\mu_i+\mu_j} \left(\frac{\mathbf{v}_{ij}\cdot\mathbf{r}_{ij}}{r_{ij}^2} \nabla\mathcal{W}_{ij} + \mathbf{r}_{ij}\times(\mathbf{v}_{ij}\times\nabla\mathcal{W}_{ij}) \right) \Delta V_j \,, \tag{C7}$$

the first term in parenthesis conserves both linear and angular momentum while the second only conserves the former. If we keep only the first term, we reproduce the artificial viscosity proposed by Monaghan (2005)

$$\langle \mathbf{f}_{\rm visc} \rangle_i = \sum_{j\in\Omega} \frac{16\mu_i\mu_j}{\mu_i+\mu_j} \frac{\mathbf{v}_{ij}\cdot\mathbf{r}_{ij}}{r_{ij}^2} \nabla\mathcal{W}_{ij}\, \Delta V_j \,, \tag{C8}$$

where a factor of 16 (rather than 4) was argued for the leading coefficient. As before, Grenier et al. (2009) propose the modification,

$$\prec \mathbf{f}_{\rm visc} \succ_i = \sum_{j\in\Omega} \frac{8\mu_i\mu_j}{\mu_i+\mu_j} \left(\frac{1}{\Gamma_i} + \frac{1}{\Gamma_j} \right) \frac{\mathbf{v}_{ij}\cdot\mathbf{r}_{ij}}{r_{ij}^2} \nabla\mathcal{W}_{ij}\, \Delta V_j \,, \tag{C9}$$

to provide a correction at the free surface. In this work, we chose to preserve angular momentum and employ Eq. (C9) for the viscosity.

APPENDIX D

Heat Conduction and the Transfer of Heat from the Environment

The heat conduction equation,

$$\frac{dU}{dt} = \frac{1}{\rho}\nabla\cdot(\kappa\nabla T) \,, \tag{D1}$$

involves the scalar Laplacian, and the derivation is identical to the viscosity. We therefore have

$$\left\langle \frac{dU}{dt} \right\rangle_i = \frac{1}{\rho_i} \sum_{j\in\Omega} \frac{4\kappa_i\kappa_j}{\kappa_i+\kappa_j} (T_i - T_j) F_{ij}\, \Delta V_j \,, \tag{D2}$$

where the identity in Eq. (A6) has been used to replace the gradient term to match the form given in Cleary and Monaghan (1999).

As discussed in Section b, to transfer heat to the snowflake from the surrounding environment requires the evaluation of

$$\sum_{j\in\Omega_{\rm air}} F_{ij}\,\Delta V_{\rm air}\,, \tag{D3}$$

without explicitly simulating air SPH-particles. To do this, we use the identity

$$\int_{\Omega_{\rm air}} F(\|\mathbf{r}-\mathbf{r}'\|)\,dV' = \int_{\Omega} F(\|\mathbf{r}-\mathbf{r}'\|)\,dV' - \int_{\Omega/\Omega_{\rm air}} F(\|\mathbf{r}-\mathbf{r}'\|)\,dV'. \tag{D4}$$

The first term on the RHS can be compute analytically, and we find

$$\int_{\Omega} F(\|\mathbf{r}-\mathbf{r}'\|)\,dV = -\left\langle \|\mathbf{r}-\mathbf{r}'\|^{-2}\right\rangle . \tag{D5}$$

The result for the Wendland C^2 kernel is given in Eq. (A8). The second term can be approximated as an SPH sum, since it is over the non air SPH-particles giving the desired result,

$$\sum_{j\in\Omega_{\rm air}} F_{ij}\,\Delta V_{\rm air} \approx -\left(\left\langle \|\mathbf{r}-\mathbf{r}'\|^{-2}\right\rangle + \sum_{j\in\Omega/\Omega_{\rm air}} F_{ij}\,\Delta V_j\right). \tag{D6}$$

To impose continuity between the interior SPH solution and exterior boundary condition, we solve

$$4\pi\kappa r_{\rm min}(T_\infty - T_{\rm air}) = \sum_{\text{all particles}} m\left\langle \frac{dU}{dt}\right\rangle \tag{D7}$$

for $T_{\rm air}$ which results in,

$$T_{\rm air} = \frac{\pi\kappa_{\rm air} r_{\rm min} T_\infty + \sum_i \frac{\kappa_i\kappa_{\rm air}}{\kappa_i+\kappa_{\rm air}}\left(\left\langle \|\mathbf{r}-\mathbf{r}'\|^{-2}\right\rangle + \sum_{j\in\Omega/\Omega_{\rm air}} F_{ij}\,\Delta V_j\right) T_i\,\Delta V_i}{\pi r_{\rm min}\kappa_{\rm air} + \sum_i \frac{\kappa_i\kappa_{\rm air}}{\kappa_i+\kappa_{\rm air}}\left(\left\langle \|\mathbf{r}-\mathbf{r}'\|^{-2}\right\rangle + \sum_{j\in\Omega/\Omega_{\rm air}} F_{ij}\,\Delta V_j\right)\Delta V_i}, \tag{D8}$$

where the sum over i is taken over all simulated SPH-particles.

APPENDIX E

Time Integration

To advance the simulation the kick-drift-kick approach proposed by Monaghan (2005) is used. Specifically, the velocities are “kicked" first as

$$\mathbf{v}_{t+\frac{1}{2}} = \mathbf{v}_t + \mathbf{a}_t \left(\frac{\Delta t}{2} \right), \tag{E1}$$

and the positions are drifted as

$$\mathbf{r}_{t+1} = \mathbf{r}_t + \mathbf{v}_{t+\frac{1}{2}} \Delta t\,, \tag{E2}$$

where $\mathbf{a}_t$ is the SPH-particle acceleration computed in the previous step. The density, volume strain rate, and forces are computed using the new positions and velocities, and the final kick is computed as

$$\mathbf{v}_{t+1} = \mathbf{v}_{t+\frac{1}{2}} + \mathbf{a}_{t+1} \frac{\Delta t}{2}\,, \tag{E3}$$

as well as the thermal and volume updates

$$\Delta V_{t+1} = \Delta V_t + \Delta V_t < \nabla \cdot \mathbf{v} > \Delta t\,, \tag{E4}$$

$$T_{t+1} = T_t + \left\langle \frac{dT}{dt} \right\rangle \Delta t\,, \tag{E5}$$

$$U_{t+1} = U_t + \left\langle \frac{dU}{dt} \right\rangle \Delta t\,. \tag{E6}$$

To set the timestep, following Morris (2000), we use the constraints,

$$\Delta t \leq 0.25 \frac{h}{c}, \tag{E7}$$

$$\Delta t \leq 0.25 \left(\frac{\rho h^3}{2\pi\sigma} \right)^{1/2}, \tag{E8}$$

$$\Delta t \leq 0.25 \left(\frac{h}{a_{\max}} \right)^{1/2}, \tag{E9}$$

$$\Delta t \leq 0.125 \frac{\rho h^3}{\mu}, \tag{E10}$$

$$\Delta t \leq 0.15 \rho c_\nu h^2 / \kappa, \tag{E11}$$

where $a_{\max}$ is the magnitude of the largest particle acceleration, and the last criteria is the thermal conduction constraint from Cleary and Monaghan (1999) where κ is taken as the largest conductivity.

References

Adami, S., X. Y. Hu, and N. A. Adams, 2012: A generalized wall boundary condition for smoothed particle hydrodynamics. *Journal of Computational Physics*, **231 (21)**, 7057–7075.

Adhikari, N. B., and K. Nakamura, 2004: An assessment on the performance of a dual-wavelength (13.6/35.0 ghz) radar to observe rain and snow from space. *Radio Science*, **39 (2)**, 1–20.

Barth, M. C., and D. B. Parsons, 1996: Microphysical processes associated with intense frontal rainbands and the effect of evaporation and melting on frontal dynamics. *Journal of Atmospheric Sciences*, **53 (11)**, 1569–1586.

Battaglia, A., C. Kummerow, D.-B. Shin, and C. Williams, 2003: Constraining microwave brightness temperatures by radar brightband observations. *Journal of Atmospheric and Oceanic Technology*, **20 (6)**, 856–871.

Bauer, P., A. Khain, A. Pokrovsky, R. Meneghini, C. Kummerow, F. Marzano, and J. P. Baptista, 2000: Combined cloud–microwave radiative transfer modeling of stratiform rainfall. *Journal of the atmospheric sciences*, **57 (8)**, 1082–1104.

Botta, G., K. Aydin, and J. Verlinde, 2010: Modeling of microwave scattering from cloud ice crystal aggregates and melting aggregates: A new approach. *IEEE Geoscience and Remote Sensing Letters*, **7 (3)**, 572–576.

Brackbill, J. U., D. B. Kothe, and C. Zemach, 1992: A continuum method for modeling surface tension. *Journal of computational physics*, **100 (2)**, 335–354.

Cholette, M., J. M. Thériault, J. A. Milbrandt, and H. Morrison, 2020: Impacts of predicting the liquid fraction of mixed-phase particles on the simulation of an extreme freezing rain event: the 1998 north american ice storm. *Monthly Weather Review*, **148 (9)**, 3799–3823.

Cleary, P. W., and J. J. Monaghan, 1999: Conduction modelling using smoothed particle hydrodynamics. *Journal of Computational Physics*, **148 (1)**, 227–264.

Colagrossi, A., M. Antuono, and D. Le Touzé, 2009: Theoretical considerations on the free-surface role in the smoothed-particle-hydrodynamics model. *Physical Review E*, **79 (5)**, 056 701.

D'Amico, M. M., A. R. Holt, and C. Capsoni, 1998: An anisotropic model of the melting layer. *Radio Science*, **33 (3)**, 535–552.

Dehnen, W., and H. Aly, 2012: Improving convergence in smoothed particle hydrodynamics simulations without pairing instability. *Monthly Notices of the Royal Astronomical Society*, **425 (2)**, 1068–1082.

Fabry, F., and W. Szyrmer, 1999: Modeling of the melting layer. part ii: Electromagnetic. *Journal of the atmospheric sciences*, **56 (20)**, 3593–3600.

Fabry, F., and I. Zawadzki, 1995: Long-term radar observations of the melting layer of precipitation and their interpretation. *Journal of the atmospheric sciences*, **52 (7)**, 838–851.

Frick, C., A. Seifert, and H. Wernli, 2013: A bulk parametrization of melting snowflakes with explicit liquid water fraction for the cosmo model. *Geoscientific Model Development*, **6 (6)**, 1925–1939.

Fujiyoshi, Y., 1986: Melting snowflakes. *Journal of Atmospheric Sciences*, **43 (3)**, 307–311.

Geresdi, I., N. Sarkadi, and G. Thompson, 2014: Effect of the accretion by water drops on the melting of snowflakes. *Atmospheric research*, **149**, 96–110.

Gingold, R. A., and J. J. Monaghan, 1977: Smoothed particle hydrodynamics: theory and application to non-spherical stars. *Monthly notices of the royal astronomical society*, **181 (3)**, 375–389.

Gravner, J., and D. Griffeath, 2009: Modeling snow-crystal growth: A three-dimensional mesoscopic approach. *Physical Review E*, **79 (1)**, 011 601.

Grenier, N., M. Antuono, A. Colagrossi, D. Le Touzé, and B. Alessandrini, 2009: An hamiltonian interface sph formulation for multi-fluid and free surface flows. *Journal of Computational Physics*, **228 (22)**, 8380–8393.

Haji-Sheikh, A., and E. M. Sparrow, 1966: The floating random walk and its application to monte carlo solutions of heat equations. *SIAM Journal on Applied Mathematics*, **14 (2)**, 370–389.

Hauk, T., E. Bonaccurso, P. Villedieu, and P. Trontin, 2016: Theoretical and experimental investigation of the melting process of ice particles. *Journal of Thermophysics and Heat Transfer*, **30 (4)**, 946–954.

Heymsfield, A. J., A. Bansemer, P. R. Field, S. L. Durden, J. L. Stith, J. E. Dye, W. Hall, and C. A. Grainger, 2002: Observations and parameterizations of particle size distributions in deep tropical cirrus and stratiform precipitating clouds: Results from in situ observations in trmm field campaigns. *Journal of the atmospheric sciences*, **59 (24)**, 3457–3491.

Heymsfield, A. J., A. Bansemer, M. R. Poellot, and N. Wood, 2015: Observations of ice microphysics through the melting layer. *Journal of the Atmospheric Sciences*, **72 (8)**, 2902–2928.

Heymsfield, A. J., A. Bansemer, A. Theis, and C. Schmitt, 2021: Survival of snow in the melting layer: Relative humidity influence. *Journal of the Atmospheric Sciences*, **78 (6)**, 1823–1845.

Iwasaki, K., H. Uchida, Y. Dobashi, and T. Nishita, 2010: Fast particle-based visual simulation of ice melting. *Computer graphics forum*, Wiley Online Library, Vol. 29, 2215–2223.

Johnson, B., W. Olson, and G. Skofronick-Jackson, 2016: The microwave properties of simulated melting precipitation particles: Sensitivity to initial melting. *Atmospheric measurement techniques*, **9 (1)**, 9–21.

Klaassen, W., 1988: Radar observations and simulation of the melting layer of precipitation. *Journal of Atmospheric Sciences*, **45 (24)**, 3741–3753.

Knight, C. A., 1979: Observations of the morphology of melting snow. *Journal of Atmospheric Sciences*, **36 (6)**, 1123–1130.

Kuo, K.-S., and C. Pelissier, 2015: Simulating ice particle melting using smooth particle hydrodynamics. *EGU General Assembly Conference Abstracts*, 6349.

Kuo, K.-S., and Coauthors, 2016: The microwave radiative properties of falling snow derived from nonspherical ice particle models. part i: An extensive database of simulated pristine crystals and aggregate particles, and their scattering properties. *Journal of Applied Meteorology and Climatology*, **55 (3)**, 691–708.

Leary, C. A., and R. A. Houze, 1979: Melting and evaporation of hydrometeors in precipitation from the anvil clouds of deep tropical convection. *Journal of the Atmospheric Sciences*, **36 (4)**, 669–679.

Leinonen, J., and A. von Lerber, 2018: Snowflake melting simulation using smoothed particle hydrodynamics. *Journal of Geophysical Research: Atmospheres*, **123 (3)**, 1811–1825.

Liao, L., and R. Meneghini, 2005: On modeling air/spaceborne radar returns in the melting layer. *IEEE transactions on geoscience and remote sensing*, **43 (12)**, 2799–2809.

Liao, L., R. Meneghini, L. Tian, and G. M. Heymsfield, 2009: Measurements and simulations of nadir-viewing radar returns from the melting layer at x and w bands. *Journal of applied meteorology and climatology*, **48 (11)**, 2215–2226.

Liu, M., J. Shao, and H. Li, 2014: An sph model for free surface flows with moving rigid objects. *International Journal for Numerical Methods in Fluids*, **74 (9)**, 684–697.

Loftus, A., W. Cotton, and G. Carrió, 2014: A triple-moment hail bulk microphysics scheme. part i: Description and initial evaluation. *Atmospheric research*, **149**, 35–57.

Lord, S. J., H. E. Willoughby, and J. M. Piotrowicz, 1984: Role of a parameterized ice-phase microphysics in an axisymmetric, nonhydrostatic tropical cyclone model. *Journal of Atmospheric Sciences*, **41 (19)**, 2836–2848.

Lucy, L. B., 1977: A numerical approach to the testing of the fission hypothesis. *The astronomical journal*, **82**, 1013–1024.

Marzano, F. S., and P. Bauer, 2001: Sensitivity analysis of airborne microwave retrieval of stratiform precipitation to the melting layer parameterization. *IEEE transactions on geoscience and remote sensing*, **39 (1)**, 75–91.

Mason, B., 1956: On the melting of hailstones. *Quarterly Journal of the Royal Meteorological Society*, **82 (352)**, 209–216.

Matsuo, T., and Y. Sasyo, 1981: Empirical formula for the melting rate of snowflakes. *Journal of the Meteorological Society of Japan. Ser. II*, **59 (1)**, 1–9.

Meneghini, R., and L. Liao, 1996: Comparisons of cross sections for melting hydrometeors as derived from dielectric mixing formulas and a numerical method. *Journal of Applied Meteorology and Climatology*, **35 (10)**, 1658–1670.

Meneghini, R., and L. Liao, 2000: Effective dielectric constants of mixed-phase hydrometeors. *Journal of atmospheric and oceanic technology*, **17 (5)**, 628–640.

Misumi, R., H. Motoyoshi, S. Yamaguchi, S. Nakai, M. Ishizaka, and Y. Fujiyoshi, 2014: Empirical relationships for estimating liquid water fraction of melting snowflakes. *Journal of Applied Meteorology and Climatology*, **53 (10)**, 2232–2245.

Mitra, S., O. Vohl, M. Ahr, and H. Pruppacher, 1990: A wind tunnel and theoretical study of the melting behavior of atmospheric ice particles. iv: Experiment and theory for snow flakes. *Journal of Atmospheric Sciences*, **47 (5)**, 584–591.

Monaghan, J. J., 1992: Smoothed particle hydrodynamics. *Annual review of astronomy and astrophysics*, **30 (1)**, 543–574.

Monaghan, J. J., 2005: Smoothed particle hydrodynamics. *Reports on progress in physics*, **68 (8)**, 1703.

Morris, J. P., 2000: Simulating surface tension with smoothed particle hydrodynamics. *International journal for numerical methods in fluids*, **33 (3)**, 333–353.

Mróz, K., A. Battaglia, S. Kneifel, L. von Terzi, M. Karrer, and D. Ori, 2021: Linking rain into ice microphysics across the melting layer in stratiform rain: a closure study. *Atmospheric Measurement Techniques*, **14 (1)**, 511–529.

Olson, W. S., P. Bauer, N. F. Viltard, D. E. Johnson, W.-K. Tao, R. Meneghini, and L. Liao, 2001: A melting-layer model for passive/active microwave remote sensing applications. part i: Model formulation and comparison with observations. *Journal of Applied Meteorology*, **40 (7)**, 1145–1163.

Olson, W. S., and Coauthors, 2016: The microwave radiative properties of falling snow derived from nonspherical ice particle models. part ii: Initial testing using radar, radiometer and in situ observations. *Journal of Applied Meteorology and Climatology*, **55 (3)**, 709–722.

Oraltay, R., and J. Hallett, 1989: Evaporation and melting of ice crystals: A laboratory study. *Atmospheric research*, **24 (1-4)**, 169–189.

Oraltay, R., and J. Hallett, 2005: The melting layer: A laboratory investigation of ice particle melt and evaporation near 0 c. *Journal of Applied Meteorology and Climatology*, **44 (2)**, 206–220.

Ori, D., T. Maestri, R. Rizzi, D. Cimini, M. Montopoli, and F. Marzano, 2014: Scattering properties of modeled complex snowflakes and mixed-phase particles at microwave and millimeter frequencies. *Journal of Geophysical Research: Atmospheres*, **119 (16)**, 9931–9947.

Panagopoulos, A. D., P.-D. M. Arapoglou, and P. G. Cottis, 2004: Satellite communications at ku, ka, and v bands: Propagation impairments and mitigation techniques. *IEEE communications surveys & tutorials*, **6 (3)**, 2–14.

Phillips, V. T., A. Pokrovsky, and A. Khain, 2007: The influence of time-dependent melting on the dynamics and precipitation production in maritime and continental storm clouds. *Journal of the atmospheric sciences*, **64 (2)**, 338–359.

Planche, C., W. Wobrock, and A. I. Flossmann, 2014: The continuous melting process in a cloud-scale model using a bin microphysics scheme. *Quarterly Journal of the Royal Meteorological Society*, **140 (683)**, 1986–1996.

811 Rasmussen, R., V. Levizzani, and H. Pruppacher, 1984: A wind tunnel and theoretical study on
812 the melting behavior of atmospheric ice particles: Iii. experiment and theory for spherical ice
813 particles of radius> 500 μm. *Journal of Atmospheric Sciences*, **41 (3)**, 381–388.

814 Rasmussen, R., and H. Pruppacher, 1982: A wind tunnel and theoretical study of the melting
815 behavior of atmospheric ice particles. i: A wind tunnel study of frozen drops of radius< 500
816 μm. *Journal of Atmospheric Sciences*, **39 (1)**, 152–158.

817 Russchenberg, H., and L. P. Ligthart, 1996: Backscattering by and propagation through the melting
818 layer of precipitation: A new polarimetric model. *IEEE transactions on geoscience and remote*
819 *sensing*, **34 (1)**, 3–14.

820 Schechter, H., and R. Bridson, 2012: Ghost sph for animating water. *ACM Transactions on Graphics*
821 *(TOG)*, **31 (4)**, 1–8.

822 Siles, G. A., J. M. Riera, and P. Garcia-del Pino, 2015: Atmospheric attenuation in wireless
823 communication systems at millimeter and thz frequencies [wireless corner]. *IEEE Antennas and*
824 *Propagation Magazine*, **57 (1)**, 48–61.

825 Stewart, R. E., J. D. Marwitz, J. C. Pace, and R. E. Carbone, 1984: Characteristics through the
826 melting layer of stratiform clouds. *Journal of Atmospheric Sciences*, **41 (22)**, 3227–3237.

827 Szeto, K., and R. Stewart, 1997: Effects of melting on frontogenesis. *Journal of the atmospheric*
828 *sciences*, **54 (6)**, 689–702.

829 Szeto, K. K., C. A. Lin, and R. E. Stewart, 1988: Mesoscale circulations forced by melting
830 snow. part i: Basic simulations and dynamics. *Journal of the atmospheric sciences*, **45 (11)**,
831 1629–1641.

832 Szyrmer, W., and I. Zawadzki, 1999: Modeling of the melting layer. part i: Dynamics and
833 microphysics. *Journal of the atmospheric sciences*, **56 (20)**, 3573–3592.

834 Tao, W., J. Scala, B. Ferrier, and J. Simpson, 1995: The effect of melting processes on the
835 development of a tropical and a midlatitude squall line. *Journal of the atmospheric sciences*,
836 **52 (11)**, 1934–1948.

Thériault, J. M., R. E. Stewart, and W. Henson, 2010: On the dependence of winter precipitation types on temperature, precipitation rate, and associated features. *Journal of applied meteorology and climatology*, **49 (7)**, 1429–1442.

Trask, N., K. Kim, A. Tartakovsky, M. Perego, and M. L. Parks, 2015: A highly-scalable implicit sph code for simulating single-and multi-phase flows in geometrically complex bounded domains. Tech. rep., Sandia National Lab.(SNL-NM), Albuquerque, NM (United States).

Tridon, F., and Coauthors, 2019: The microphysics of stratiform precipitation during olympex: Compatibility between triple-frequency radar and airborne in situ observations. *Journal of Geophysical Research: Atmospheres*, **124 (15)**, 8764–8792.

Tyynelä, J., J. Leinonen, D. Moisseev, T. Nousiainen, and A. von Lerber, 2014: Modeling radar backscattering from melting snowflakes using spheroids with nonuniform distribution of water. *Journal of Quantitative Spectroscopy and Radiative Transfer*, **133**, 504–519.

Unterstrasser, S., and G. Zängl, 2006: Cooling by melting precipitation in alpine valleys: An idealized numerical modelling study. *Quarterly Journal of the Royal Meteorological Society: A journal of the atmospheric sciences, applied meteorology and physical oceanography*, **132 (618)**, 1489–1508.

von Lerber, A., D. Moisseev, J. Leinonen, J. Koistinen, and M. T. Hallikainen, 2014: Modeling radar attenuation by a low melting layer with optimized model parameters at c-band. *IEEE Transactions on Geoscience and Remote Sensing*, **53 (2)**, 724–737.

Walden, C., G. Kuznetsov, and A. Holt, 2000: Topology-dependent modelling of microwave scattering from melting snowflakes. *Electronics Letters*, **36 (17)**, 1494–1496.

Willis, P. T., and A. J. Heymsfield, 1989: Structure of the melting layer in mesoscale convective system stratiform precipitation. *Journal of Atmospheric Sciences*, **46 (13)**, 2008–2025.

Yokoyama, T., and H. Tanaka, 1984: Microphysical processes of melting snowflakes detected by two-wavelength radar part i. principle of measurement based on model calculation. *Journal of the Meteorological Society of Japan. Ser. II*, **62 (4)**, 650–667.

Zawadzki, I., W. Szyrmer, C. Bell, and F. Fabry, 2005: Modeling of the melting layer. part iii: The density effect. *Journal of the atmospheric sciences*, **62 (10)**, 3705–3723.

865 Zhang, W., S. I. Karhu, and E. T. Salonen, 1994: Predictions of radiowave attenuations due to a
866 melting layer of precipitation. *IEEE transactions on antennas and propagation*, **42 (4)**, 492–500.